Spring 5-15-2017

Tissue Damage Quantification in Alzheimer's Disease Brain via Magnetic Resonance Gradient Echo Plural Contrast Imaging (GEPCI)

Yue Zhao
Washington University in St. Louis

WASHINGTON UNIVERSITY IN ST. LOUIS

Department of Chemistry

Dissertation Examination Committee:
Joseph Ackerman, Chair
Alexander Barnes
Anne Cross
Dewey Holten
Dmitriy Yablonskiy

Tissue Damage Quantification in Alzheimer's Disease Brain via Magnetic Resonance Gradient Echo Plural Contrast Imaging (GEPCI)

by

Yue Zhao (赵越)

A dissertation presented to
The Graduate School
of Washington University in
partial fulfillment of the
requirements for the degree
of Doctor of Philosophy

May 2017
St. Louis, Missouri

Table of Contents

List of Figures

List of Tables

Acknowledgments

Many people provided me lots of guidance, advice, help and encouragements through my five years' Ph.D. Herein, I would like to acknowledge them in this dissertation.

I sincerely thank my two advisors Prof. Dmitriy Yablonskiy and Prof. Joseph Ackerman. I received the anytime world-class research guidance from Prof. Yablonskiy throughout my Ph.D. He taught me MRI with great patience and shared with me his 30 years' research experience. He let me understand how to become a passionate, knowledgeable, and persistent scientist. Prof. Ackerman welcomed me to Biological Magnetic Resonance Laboratory (BMRL) and supported me to pursue research directions as I wanted. He regularly discussed my projects to keep me on the right track. He always encouraged me to follow my passion because this is my degree.

I thank my dissertation committee members, Prof. Anne Cross, Prof. Dewey Holten, and Prof. Alexander Barnes for their time and advice. I thank Prof. Marcus Raichle, Prof. Jason Hassenstab, Prof Nigel Cairns, Dr. Jon Christensen for making my research move forward.

I thank Prof. Sheng-Kwei (Victor) Song for supporting me to transfer labs due to my interest. I thank Dr. Jie Wen and Dr. Jie Luo for helping me with MRI fundamentals and data processing. Many thanks to both current and past BMRL members for being around and supporting me.

I thank Prof. John Morris, Prof. Andrei Vlassenko's lab, Prof. Tammy Benzinger's lab, ADRC staff and CCIR technicians for helping me recruit AD volunteers and complete MRI scans.

My sincere gratitude to all the participants in my projects. I hope my work would make small contribution to the Alzheimer research, which may relieve patients' suffering in the future.

This dissertation is funded by the Washington University ICTS grant UL1 TR000448 from the NIH National Center for Advancing Translational Sciences, NIH grants P50AG05681, P01AG03991, and 1R01NS055963, and NMSS grant RG 4463A18.

My sincere thanks to all the friends around me for making me laugh a lot in this new country.

Lastly, I thank my parents for everything when I am not around.

Yue Zhao (赵越)

Washington University in St. Louis

May 2017

ABSTRACT OF THE DISSERTATION

Tissue Damage Quantification in Alzheimer's Disease Brain via Magnetic Resonance Gradient Echo Plural Contrast Imaging (GEPCI)

by

Yue Zhao (赵越)

Doctor of Philosophy in Chemistry

Washington University in St. Louis, 2017

Professor Joseph Ackerman, Chair

Professor Dmitriy Yablonskiy

Alzheimer's disease (AD) affected approximately 48 million people worldwide in 2015. Its devastating consequences have stimulated an intense search for AD prevention and treatment. Clinically, AD is characterized by memory deficits and progressive cognitive impairment, leading to dementia. Over the past two to three decades, researchers have found that amyloid-beta (Aβ) plaques and neurofibrillary tau tangles occur during a long pre-symptomatic period (preclinical stage) before the onset of clinical symptoms. As a result, identification of the preclinical stage is essential for the initiation of prevention trials in asymptomatic individuals. Currently, Positron Emission Tomography (PET) imaging with injected ^{11}C or ^{18}F containing radiotracers (e.g., Pittsburgh compound B, PiB or florbetapir-fluorine-18, ^{18}F-AV-45) is widely used to detect amyloid deposition *in vivo* and to identify this preclinical stage. However, PET scans are time consuming (about 1 hour), require injection of a radiotracer, thus, exposing the patient to ionizing radiation. After the preclinical stage, AD patients begin to show clinical symptoms, referred as a very mild or mild AD group. Post-mortem studies show that neuronal damage is the most proximate pathological substrate of cognitive impairment in AD compared

with amyloid and tau deposition. Thus, a diagnostic tool is needed for detection of neuronal loss *in vivo*. As a faster, non-invasive, and radiation free imaging technique, Magnetic Resonance Imaging (MRI) plays an important role in the diagnosis of cognitive diseases. Conventional MRI yields superb definition of brain anatomy and structure and provide important volumetric information (e.g., brain atrophy). However, conventional MRI cannot provide microstructural and functional insight into the pathology of AD.

The approach developed in Yablonskiy's lab is based on the Gradient Echo Plural Contrast Imaging (GEPCI) protocol, which provides quantitative *in vivo* measurements of transverse relaxation properties of the tissue water ^{1}H spins as determined from the gradient echo MRI signal. The measurements are corrected for macroscopic magnetic field inhomogeneity effects and physiologic-motion-driven fluctuations in magnetic field as these are the major artifacts present with the gradient echo technique. The principal relaxation property used in this dissertation is the tissue-specific transverse relaxation rate constant, R2*. The R2* value reflects the microscopic and mesoscopic magnetic field inhomogeneities rising from the complex tissue-water-environment within the human brain. In turn, changes in R2* reflect changes in the tissue's microscopic and mesoscopic tissue structure.

However, because of the presence of the cerebral blood vessel network, the magnetic-susceptibility-driven blood-oxygen-level dependent (BOLD) effect also makes a significant contribution to R2*. A previously developed approach, quantitative BOLD (qBOLD), allows the separation of R2* into a tissue specific R2t* without blood vessel effects and the BOLD component. Quantifying the BOLD component allows the calculation of cerebral hemodynamics parameters, such as oxygen extraction fraction (OEF) and deoxygenated cerebral blood volume

(dCBV). These parameters (R2*, R2t*, OEF, dCBV) describe structural and functional properties of tissue at the microstructural level in the human brain.

In the study of normal aging, quantitative GEPCI measurements showed that R2t* increases with age while hemodynamic parameters, i.e., relative OEF and dCBV remain constant in most cerebral cortical regions. The comparison between quantitative GEPCI measurements and literature information suggest that (a) age-related increases in the cortical R2t* mostly reflect the age-related increases in the cellular packing density (or neuronal density); (b) regions in a brain characterized by higher R2t* contain a higher concentration of neurons with less developed cellular processes (dendrites, spines, etc.); and (c) brain regions characterized by lower R2t* represent regions with lower concentration of neurons but more developed cellular processes.

In the Alzheimer study, R2* and R2t* together demonstrated significant differences among the normal, preclinical and mild AD groups. First, the results uncovered strong correlations between R2* and Aβ deposition measured by the PiB PET-tracer in several cortical regions (e.g., medial temporal lobe and precuneus). This finding indicates that R2* may be a potential surrogate marker for Aβ deposition. The strongest correlation was found in the medial temporal lobe (MTL), particularly in the parahippocampal cortex, which can be used to distinguish the normal and preclinical groups.

Second, R2t* in the hippocampus, which characterized the hippocampal cellular integrity demonstrated much stronger correlations with psychometric tests than volume quantification of hippocampal atrophy. Importantly, decreased R2t* characterizing cellular damage was detected even in the hippocampal areas not affected by atrophy. In addition, R2t* significantly decreased in the mild AD group but was preserved in the preclinical group compared with the normal

group. These results indicate a significant cellular density decrease in the mild group but not in the preclinical group, which is consistent with previous histological studies.

In summary, GEPCI provides a new approach for evaluation of AD-related tissue pathology *in vivo* in the preclinical and early symptomatic stages of AD. Since MRI is widely available worldwide and does not require radiation exposure, it provides the opportunity to obtain new information on the pathogenesis of AD and for pre-screening cohorts (stratification) for clinical drug trials.

Chapter 1: Introduction to Gradient Echo Plural Contrast Imaging (GEPCI)

1.1 MRI Basics

1.1.1 Nuclear Spins

In classic physics, a rotating object possesses a property known as angular momentum. The angular momentum is related to the object's size, mass, and rotational velocity. However, in quantum mechanics, spin or spin angular momentum is an intrinsic property of atomic and subatomic particles. The quantum spin number *s* is quantized, which means that it only takes values of N/2, where *N* is a non-negative integer. So the spin angular momentum *S* of any physical system is also quantized with the spin quantum number *s* and Planck's constant *h*:

$$S = \frac{h}{2\pi}\sqrt{s(s+1)} \ . \tag{1.1}$$

The component of *S* along any direction is calculated as follows:

$$S_i = \frac{h}{2\pi} s_i, s_i \in \{-s, -s+1, ..., s-1, s\} . \tag{1.2}$$

Thus, we see that *S* has 2*s*+1 components in different directions.

Due to the intrinsic spin, particles also have an intrinsic magnetic moment μ, which is the product of the gyromagnetic ratio γ and the spin angular momentum *S*:

$$\mu = \gamma S \ . \tag{1.3}$$

The magnetic moment is used to describe how a small magnetic dipole (or current loop) interacts with an external magnetic field. The magnetic energy of a particle (E) is the dot product of its magnetic moment and the external magnetic field (B_0):

$$E = -\vec{\mu} \cdot \vec{B_0} \ . \tag{1.4}$$

Let us take the proton as an example, because it is the most common source of MRI signal. The quantum spin number s of a proton is ½. So there are $2 \times \frac{1}{2} + 1 = 2$ components of the spin angular momentum S. Assume that B_0 is applied along the Z direction and substitute μ with γ and S. Then the magnetic energy (E) of protons is written as follows:

$$E = -\gamma S_z B_0 = \pm \frac{h}{4\pi} \gamma B_0 \, . \tag{1.5}$$

We see that proton has two energy states in the presence of an external magnetic field (also referred to spin-up and spin-down). The energy difference between the two states is written as follows:

$$\Delta E = \frac{h}{2\pi} \gamma B_0 \, . \tag{1.6}$$

According to Boltzmann statistics, the population ratio of the spins in the two states is calculated as follows:

$$\frac{Population(anti-parallel)}{Population(parallel)} = \exp(-\frac{\Delta E}{kT}) = \exp(-\frac{h\gamma B_0}{2\pi kT}) \ , \tag{1.7}$$

where k is the Boltzman constant and T is the absolute temperature. At body temperature in a field of 3.0 Tesla, the population ratio is nearly 1. Only a small excess on the order of 1 per 10^6

spins is expected to be found in the lower energy state. Fortunately, in a biological environment, there is a large enough population of ^{1}H to provide a sufficient MRI signal.

1.1.2 Free Induction Decay (FID) Signal

For convenience, in the field of magnetic resonance imaging, nuclear spins are usually considered as the analogue of spins in classical physics. Thus, spins are considered to precess around the magnetic field B_0. The frequency of the precession is known as the Larmor frequency:

$$\omega_0 = \gamma B_0 \ . \tag{1.8}$$

We see that ΔE is proportional to the Larmor frequency as well, which is the frequency required for the transition of the two energy states. Spins at equilibrium produce a net magnetization M_0 along B_0. It is convenient to use this net magnetization M_0 to interact with B_0 instead of considering all the spins.

To understand the formation of the MRI signal, let us define a space with X, Y, and Z directions. The external magnetic field, B_0, is along the Z direction. In reality, the receiver coils are placed on the transverse plane to detect the currents generated by the precession of the transverse magnetization around B_0. Thus, an electromagnetic radio frequency (RF) pulse with a nearly Larmor frequency is usually applied perpendicular to B_0 to flip M_0 towards the XY plane by a certain angle. At the quantum level, nuclear spins absorb the energy from the RF pulse with Larmor frequency and are excited to the higher energy state. After the RF pulse is turned off, two independent relaxations, T1 and T2* relaxations, occur simultaneously. A T1 relaxation is also called a thermal relaxation, in which the spins release the absorbed energy to the surrounding environment and return to the thermal equilibrium. As a result, the Z component (M_z) of the magnetization grows back to M_0 over time. For example, consider a 90° RF pulse that is applied

to flip M_0 onto the transverse plane. After the RF pulse is turned off, M_z changes over time (t) in accord with the following equation:

$$M_z = M_0 \cdot (1 - \exp(-t / T_1)) \ . \tag{1.9}$$

In the meantime, the nuclear spins start to dephase on the transverse plane due to magnetic-field inhomogeneities—a process that is characterized as a T2* relaxation. The inhomogeneities include irreversible and reversible parts. The irreversible part is caused by the fluctuating magnetic fields generated from the spin-spin interactions—a process that is characterized as a T2 relaxation. There are three sources that induce a microscopic inhomogeneous field on the atomic level: electron spin, electron orbital current, and nucleus spin. The reversible part is mainly due to external fixed inhomogeneities, such as imperfect magnet and field distortion at the air/tissue interface. The transverse magnetization ($M_{x,y}$) changes over time t, as in the following equation:

$$M_{x,y} = M_0 \cdot \exp(-t / T_2^*) \cdot \cos(\omega_0 \cdot t + \varphi_0) . \tag{1.10}$$

Due to T2* relaxation, the transverse magnetization $M_{x,y}$ decays over time, which is referred to as a free induction decay (FID) signal.

1.1.3 Gradients, Gradient Echo Sequence and K-Space

Although the FID can be measured, the signal comes from the whole object, and the signal at each location on the object needs to be computed. Thus, a constant magnetic field gradient is applied so that the overall magnetic field is linearly dependent on the location. For example, consider a one-dimensional situation: The homogeneous magnetic field B_0 is along the X direction, and a gradient G_x is applied along the same direction. Then the distribution of the overall magnetic field is linearly dependent on the location x:

$$B = B_0 + G_x \cdot x \ . \tag{1.11}$$

Accordingly, the precession frequency is dependent on the location *x*:

$$\omega = \gamma B = \omega_0 + \gamma \cdot G_x \cdot x \ . \tag{1.12}$$

As a result, the location of a proton is encoded by its precession frequency, which is known as frequency encoding. Frequency encoding provides a one-dimensional projection of spin density.

To get a two-dimensional image, we need to apply a gradient (G_y) in the orthogonal direction (e.g., the Y direction) to the frequency-encoding gradient, which is known as the phase-encoding gradient. The phase-encoding gradient is applied after the RF pulse and before the frequency-encoding gradient for a short period (on the order of millisecond). In this short duration, spins accumulate a certain amount of phase to encode the location along Y direction. Likewise, a three-dimensional image is created by adding an additional phase-encoding gradient along the Z direction. The location along the Y and Z directions is encoded by the accumulated phase, while the location along X is encoded by the precession frequencies.

Because all of the MRI experiments in my projects are based on the gradient echo (GE) sequence, a diagram of the sequence to obtain a 2-D MRI image is shown below in Figure 1.1:

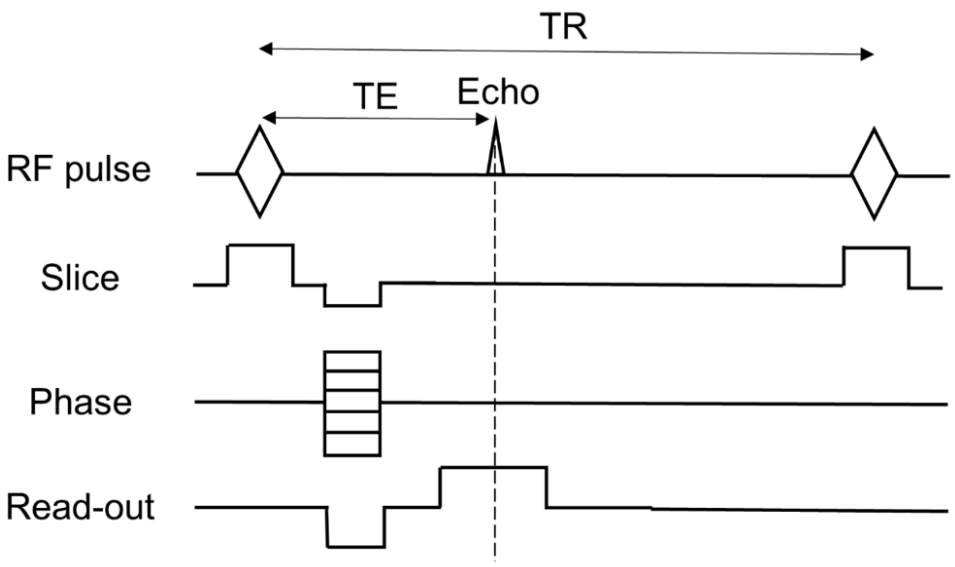

Figure 1.1 A diagram of the gradient echo sequence to obtain a 2-D MRI image.

First, a frequency-selective RF pulse is applied to flip the original magnetization M_0 by a certain angle (30° in GEPCI experiments). Concurrently, a slice-selective gradient is applied along the slice direction (the Z direction) to excite spins in a targeting slice. However, the gradient brings magnetic-field inhomogeneity and causes unwanted dephasing of the spins, which starts in the middle of RF pulse duration. Thus, a rewinding gradient with exactly half the power of the slice gradient follows to refocus the spins. Then a single step of the phase-encoding gradients is applied over a certain duration to let the spins accumulate spatially dependent phase along the Y direction. Next, a pre-rewind gradient is applied over exactly half of the read-out duration (t/2) along the X direction. Then the readout gradient is turned on to refocus the spins and form an echo at the gradient echo time (TE). In the meantime, the signal receiver is also turned on to sample signals over time. The signal sampled during one read-out gradient is a single line of the k-space. The same procedure is repeated at every time of repetition (TR) to fill in lines in k-space. Notice that, in every repetition, the phase-encoding gradients move to the next step (a new

gradient). When all of the repetitions are completed, the phase-encoding gradients move to the last step and the k-space is fully filled. To obtain a 3-D image, replace the slice-selective gradient with an additional phase-encoding gradient.

Assume that there is no other magnetic-field inhomogeneity except for the gradients along the XYZ directions. The signal at each point during the read-out sampling can then be written as,

$$\tilde{S}(t) = \iiint_{x,y,z} \rho(x,y,z) \cdot \exp[i\omega_0(TE+t) - i\gamma G_x xt - i\gamma G_y y t_y - i\gamma G_z z t_z] \cdot dxdydz , \qquad (1.13)$$

where $\rho(x,y,z)$ is the "ideal" signal at location (x, y, z) on the object. Notice the time is represented as *TE+t*, where *t* is the time during GE acquisition (*t* is zero at the center of the GE). To compute $\rho(x,y,z)$, we substitute $2\pi k_j = \gamma G_j t_j (j = x,y,z)$, and the equation is rewritten as follows:

$$\tilde{S}(k_x,k_y,k_z) = \iiint_{x,y,z} \rho(x,y,z) \cdot \exp[i\omega_0(TE+t) - 2\pi k_x x - 2\pi k_y y - 2\pi k_z z] \cdot dxdydz . \qquad (1.14)$$

$\tilde{S}(k_x,k_y,k_z)$ is the so called "k-space". In GEPCI experiments, the k-space at each slice is comprised of 256 lines, and each line is comprised of 256 points. Notice that k-space is the 3D Fourier transform of the signal in the image domain $\rho(x,y,z)$. So inverse Fourier transform is applied to the k-space data to generate $\rho(x,y,z)$:

$$\rho(x,y,z) = FT^{-1}[\tilde{S}(k_x,k_y,k_z)] . \qquad (1.15)$$

But in reality, the sampling during read-out duration is discrete. As a result, the signals in both the k-space and the image domain are stored in voxels (k_x, k_y, k_z are integers). The signal within a voxel is considered an integral over the locations. Thus, a fast Fourier transform (FFT) algorithm is used in this case. Then the transformed image also stores signals in voxels. Different notations would be used to distinguish the signal at a continuous point and a voxel.

1.2 Gradient Echo Plural Contrast Imaging (GEPCI)

The GEPCI technique is based on, (***i***) a 3D gradient echo (GE) sequence with multiple gradient echoes (currently available from most MRI scanner manufacturers), and (**ii**) a set of post-processing algorithms (1-6) that make it possible to generate images and quantitative maps with several contrasts that reflect the anatomic and microstructural properties of biological tissue. Importantly, all these GEPCI images are simultaneously acquired and are thus naturally co-registered.

1.2.1 MRI Data Acquisition

The scans were made in a 3T PET-MR scanner (Siemens, Erlangen, Germany). A 3D multi GE sequence and a 12-channel phased-array head coil were used to obtain the data. The sequence parameters were as follows: resolution 1×1×2 mm^3 (read, phase, slab), FOV 256 mm×192 mm, repetition time TR = 50ms, flip angle 30°, 10 gradient echoes with first gradient echo time TE_1 = 4 ms, and echo spacing ΔTE = 4ms. An additional phase stabilization echo (the navigator data) was collected for each line in k-space to correct for image artifacts due to the physiological fluctuations (4). The total acquisition time of GEPCI was 11 mins 30s.

1.2.2 Image Construction by Combining Multi-channel Data

Notice that MRI data is collected through a 12-channel RF coil. After the multi-channel data was transformed from k-space to the image space by using inverse FFT, it was combined using the following algorithm (2):

$$S_n(TE) = \sum_{ch=1}^{M} \lambda_{ch} \cdot \overline{S}_n^{ch}(TE_1) \cdot S_n^{ch}(TE); \quad \lambda_{ch} = \frac{1}{M \cdot \varepsilon_{ch}^2} \sum_{ch'=1}^{M} \varepsilon_{ch'}^2 , \tag{1.16}$$

where the sum was taken over all M channels (ch), S_n represents the signal at the nth voxel in the image domain ($\tilde{S}$ is the signal in the k-space), $\overline{S}$ denotes complex conjugate of S , λ_{ch} are weighting parameters, and ε_{ch} are noise amplitudes (r.m.s.) outside the human skull on the MRI image. Index n corresponds to the voxel position. This algorithm allows for the optimal estimation of quantitative parameters (2, 7) and removes the initial phase incoherence among the channels (2).

Notice that we previously used $\rho(x, y, z)$ to denote the "ideal" signal at location (x, y, z) in the image domain. Herein, we use S_n to represent the signal at a single voxel. It is not "ideal" because of the effects of magnetic inhomogeneity.

1.2.3 Voxel Spread Function for Macroscopic Field Inhomogeneity Effects

Although gradient echo sequence is fast, the images can be adversely biased by macroscopic magnetic-field inhomogeneities. So $S_n(TE)$ includes not only the "ideal" signal within the voxel, but also the signal due to magnetic-field inhomogeneities. Yablonskiy's lab reanalyzed a basic theory of gradient echo MRI signal formation and developed a voxel spread function to model the signal behavior in the presence of macroscopic magnetic-field inhomogeneities (3). For

example, Figure 1.2 shows that this function can significantly reduce artifacts on *in vivo* MRI images due to the macroscopic magnetic-field inhomogeneity at the air/water interface.

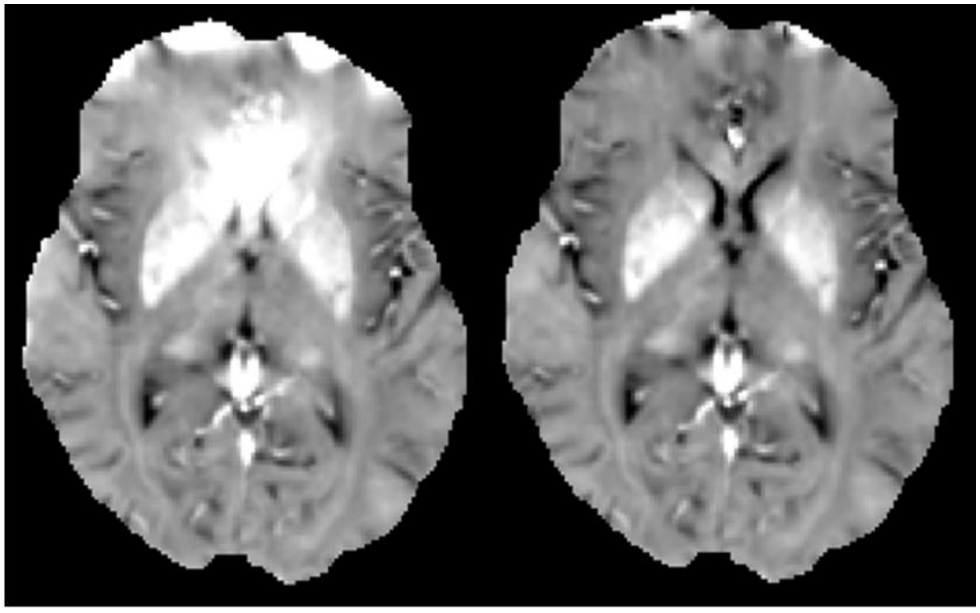

Figure 1.2 Example of an R2* map corrected with and without the voxel spread function from a healthy individual. Obviously, huge artifacts appear on the uncorrected R2* map on the left due to the macroscopic magnetic-field inhomogeneity at the air/water interface (around nose). The artifacts disappeared (right image) after the voxel spread function was applied.

The theory of this algorithm is briefly introduced here. Consider a 1-dimensional GE experiment. In the presence of an inhomogeneous magnetic field $b(x)$, the MRI signal during the readout period *t* is expressed in the following equation:

$$\tilde{S}(k_x;TE) = \int \rho(x;TE)\cdot\exp[-2\pi i k_x x + i\gamma b(x)(TE+t) + i\varphi_0(x)]\cdot dx, \qquad (1.17)$$
$$2\pi k_x = \gamma G_x t_x$$

where *TE* is the gradient echo time, *x* is the location in the image space, k_x is a voxel in k-space, G_x is the read-out gradients, t_x is the duration of the gradient, $\rho(x;TE)$ is the "ideal" signal at the

continuous location x in the absence of magnetic-field inhomogeneities, and $\varphi_0(x)$ is the signal phase shift at TE=0 (which results mainly from RF field inhomogeneities). Notice again that the time is represented as $TE+t$, where t is the time during GE acquisition (t is zero at the center of the GE).

The goal is to compute the "ideal" signal in a voxel, so we need to convert the continuous equation to a discrete equation on the voxel level. Because the scale of macroscopic field inhomogeneities is much larger than the size of a voxel, the distribution of $b(x)$ and $\varphi_0(x)$ in the mth voxel is represented as a linear approximation:

$$\begin{aligned} b_m(x) &= b_m + g_{mx}x \\ \varphi_0(x) &= \varphi_{0,m} + \varphi_{mx}x \end{aligned}, \qquad (1.18)$$

where b_m and $\varphi_{0,m}$ are constants within the mth voxel but vary over voxels, and where g_{mx} and φ_{mx} are the background gradients within the mth voxel. The "ideal" signal in the mth voxel $\sigma_m(TE)$ is represented as a sum of $\rho(x;TE)$ across the volume (V) of the voxel:

$$\sigma_m(TE) = V \cdot < \rho(x;TE) >_m , \qquad (1.19)$$

where $< \rho(x;TE) >_m$ is the averaged signal in the mth voxel. So the signal is first integrated across x in a single voxel and then the integral is substituted into Equation (1.17) with summations of voxels:

$$\begin{aligned} &\tilde{S}(k_x;TE) = \sum_m \sigma_m(TE) \cdot \exp(-2\pi i k_x x) \cdot \exp(+i\gamma b_m \cdot TE + i\varphi_{0,m}) \cdot \mathrm{sinc}[(k_x - k_{mx})a_x] \\ &2\pi k_{mx} = \gamma g_{mx} TE + \varphi_{mx} \end{aligned} . \qquad (1.20)$$

Inverse Fourier transform is applied to transform the k-space to an image domain. Thus, we have the expression for the signal at the *n*th voxel in the image domain corrected for the macroscopic magnetic-field inhomogeneity:

$$S_n(TE) = \frac{1}{N}\sum_m \{\sigma_m(TE)\cdot \exp(+i\gamma b_m TE + i\varphi_{0,m})\cdot \sum_j \mathrm{sinc}(k_{x,j}a_x - k_{mx}a_x)\cdot \exp[2\pi i k_{x,j}a_x(n-m)]\}\,. \quad (1.21)$$

In general, the overall signal in the *n*th voxel is determined by all the voxels in the image domain, including the "ideal" signal ($\sigma_m(TE)$), the accumulated phase due to the local macroscopic magnetic inhomogeneity ($b_m, \varphi_{0,m}$), and the interactions between a certain voxel and other voxels (the sinc function part).

To make this algorithm computationally feasible, we have another approximation that the signals from neighboring voxels evolve similarly over time in the absence of magnetic-field inhomogeneities so that,

$$\sigma_m(TE) = \sigma_n(TE)\frac{|S_m(TE=0)|}{|S_n(TE=0)|}\,. \quad (1.22)$$

Under this approximation, we can extract $\sigma_n(TE)$ from the sum and reduce Equation (1.21) to,

$$S_n(TE) = \sigma_n(TE)\cdot F_n(TE)$$
$$F_n(TE) = \frac{1}{|S_n(0)|}\cdot \sum_m |S_m(0)|\cdot \exp(+i\gamma b_m TE + i\varphi_{0,m})\cdot \sum_j \mathrm{sinc}(k_{x,j}a_x - k_{mx}a_x)\cdot \exp[2\pi i k_{x,j}a_x(n-m)]$$
$$. \quad (1.23)$$

where the F function $F_n(TE)$ is the voxel spread function describing the influence of macroscopic magnetic-field inhomogeneities at the *n*th voxel on the MRI image. The F-function can also be extended to 2D or 3D versions. To finish the computation projects in a reasonable

time, we used only neighboring voxels of the target voxel to compute $F_n(TE)$ instead of using all the voxels.

1.2.4 Basic GEPCI Images (T1-weighted and R2*)

With the signals in the image space $S(TE)$, the voxel spread function $F(TE)$ and a series of TEs, the standard R2* = 1/T2* map, and a T1-weighted (A_0) image and frequency (Δf) map will be produced by fitting the following equation to experimental data on a voxel basis:

$$S(TE) = A_0 \cdot \exp\left(-R2^* \cdot (TE + TE_1) + i \cdot 2\pi \cdot \Delta f \cdot (TE - TE_1)\right) \cdot F(TE), \qquad (1.24)$$

where *TE* is the gradient echo time, Δf is the frequency shift (dependent on tissue structure and also on the macroscopic magnetic field created mostly by tissue/air interfaces), and where the function *F(TE)* describes the effects of macroscopic magnetic-field inhomogeneities (8). We use a voxel spread function (VSF) method (3) to calculate *F(TE)*.

Derived contrast images can also be constructed by using the same acquisition data according to (6). But they are not used in the current projects.

1.3 Quantitative Blood-oxygen-level Dependent (BOLD) Imaging

1.3.1 Blood-oxygen-level Dependent (BOLD) Effect

R2* is a good quantitative measurement for evaluating microstructural tissue properties. However, except for the effect of the macroscopic magnetic-field inhomogeneity, there are more complicated and subtle susceptibility effects in the tissue-water environment. Unlike the macroscopic effect that biases the data, these susceptibility effects may provide interesting

information about the tissue on the cellular level. One of the most important susceptibility effects on the MRI signal is the blood-oxygen-level dependent (BOLD) effect discovered by Ogawa in 1990 (9). The paramagnetic deoxyhemoglobin in blood vessels causes additional FID signal decay. Hemoglobin (Hb or Hgb) is a type of protein in red blood cells that contains iron and transports oxygen. When it carries oxygen from respiratory organs, it becomes diamagnetic oxyhemoglobin, the susceptibility of which is about -9 ppm, similar to that of water molecules in the soft tissue. When it releases the oxygen to provide energy and collects the resultant carbon dioxide back into the respiratory organs, it becomes paramagnetic deoxyhemoglobin with a susceptibility of about 0.15 ppm. The difference of the magnetic susceptibility distorts the local magnetic field and generates the BOLD contrast.

One of the most important applications of the BOLD effect focuses on temporal changes in the MR signal during changes in brain activity, which is also known as function MRI (fMRI). Furthermore, the quantitation of the BOLD signal can provide information about the concentration of deoxyhemoglobin, which depends primarily on the oxygen extraction fraction (OEF) and the deoxygenated cerebral-blood volume (dCBV). This allows the BOLD contrast to be useful in understanding brain activities. However, the only clinically accepted OEF measurement relies on PET techniques (10), which are limited in human study and clinical practice due to their low spatial resolution and exposure to radiation.

A quantitative MRI-based approach has been developed to analytically describe the MRI signal in the presence of a blood vessel network in the static dephasing regime (11). At first, this approach was developed to evaluate the NMR signal in the presence of magnetic inclusions, such as a blood vessel network, bone marrow, and a ferrite contrast agent. There are some common behaviors for all the systems. If the echo time TE is less than a characteristic time t_c for a given

system, the signal decays exponentially with an argument which depends nonlinearly on TE. When TE is greater than t_c, the signal follows a simple exponential decay and the relaxation rate does not depend on the echo time.

This approach was used to separate tissue-specific R2t* and BOLD-related contributions from the total R2* relaxation (5, 12). The results for OEF, dCBV, and the concentration of deoxyhemoglobin in the gray matter can also be robustly calculated using this approach. The mean values of OEF and dCBV are 47% and 4.6%, respectively, which is in reasonable agreement with the literature (5).

Several studies have been published to validate different aspects of this approach. Specifically, we have developed a theoretical model of the BOLD effect (11), validated it in phantom studies (8), conducted detailed measurements of blood magnetic susceptibility (13), validated the BOLD model *in vivo* using a rat model (14), and provided an analysis of systematic errors due to diffusion effects (15) and errors due to noise in the data (12, 16)

1.3.2 qBOLD Model for Magnetic Inclusions in the Static Dephasing Regime

Notice that this approach was developed on the assumption of a static dephasing regime in which diffusion may be ignored (11). In general, the diffusion phenomena would average out the phases of different nuclei. If NMR signal decay caused by magnetic moment dephasing occurs faster than diffusion—which means that the signal would decay before the diffusion averages the dephasing—then we are in the so-called static dephasing regime. If the water-diffusion coefficient D=1 $\mu m^2/ms$ and the transverse size of blood vessel is ~10 μm, it takes 100 ms to diffuse around a blood vessel. We can treat water molecules as static in the scan time (<40 ms). That is a mesoscopic scale. On the microscopic scale, a transverse size of a molecule may be ~10A, so the water molecule would diffuse around and average the phase out before the signal is

measured. Thus, the diffusion needs to be considered, and we can treat the medium (water molecules, other small molecules) as a whole.

1.3.3 qBOLD Model for the Blood Vessel Network

Another major assumption is to model blood vessels as a set of cylinders with infinite length and arbitrary radiuses that are randomly distributed in the medium. The signal behavior in the presence of BOLD effect is then shown in $F_{BOLD}(TE)$ (11):

$$F_{BOLD}(TE) = \exp[-\zeta \cdot f_s(\delta\omega \cdot TE)] \ . \tag{1.25}$$

In practice, instead of the original function (11), we use a recently proposed expression (5),

$$F_{BOLD}(TE) = 1 - \frac{\zeta}{1-\zeta} \cdot f_s(\delta\omega \cdot TE) + \frac{1}{1-\zeta} \cdot f_s(\zeta \cdot \delta\omega \cdot TE) \ , \tag{1.26}$$

that better accounts for the presence of large vessels in the voxel than traditional exponential function (11). ζ is the deoxygenated cerebral-blood volume fraction (dCBV), and $\delta\omega$ is the characteristic frequency determined by the susceptibility difference between deoxygenated blood and surrounding tissue (11):

$$\delta\omega = \frac{4}{3}\pi \cdot \gamma \cdot B_0 \cdot Hct \cdot \Delta\chi_0 \cdot (1-Y) \ . \tag{1.27}$$

In this equation, $\Delta x_0 = 0.27\,ppm$ (13) is the susceptibility difference between fully oxygenated and fully deoxygenated blood, Y is the blood oxygenation level (with Y=0 being fully deoxygenated), Hct is the blood hematocrit, and γ is the gyromagnetic ratio. Function f_s describes the signal decay caused by the presence of the blood vessel network, which was

defined in (11). Herein we use a mathematical expression in terms of a generalized hypergeometric function ${}_1F_2$ (17):

$$f_s(\delta\omega \cdot TE) = {}_1F_2\left(\left[-\frac{1}{2}\right];\left[\frac{3}{4},\frac{5}{4}\right];-\frac{9}{16}(\delta\omega \cdot TE)^2\right)-1\ . \qquad (1.28)$$

This function has an interesting behavior. The function is nonlinear when $\delta\omega \cdot TE \leq 1$ and linear when $\delta\omega \cdot TE >> 1$, as is shown in Figure 1.3.

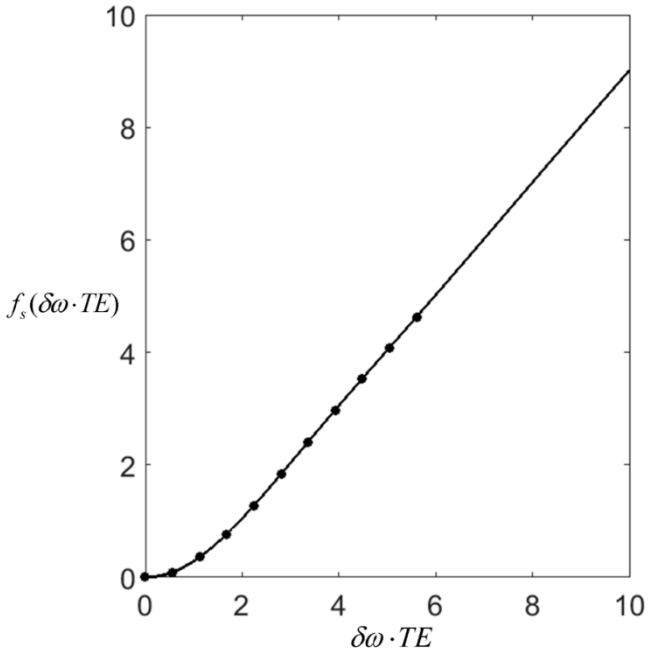

Figure 1.3 The non-linearity of function $f_s(\delta\omega \cdot TE)$ versus $\delta\omega \cdot TE$ when $\delta\omega \cdot TE \leq 1$. The dots are values at the time of echos (t = TE_n) assuming Y = 60%.

Oxygen extraction fraction (OEF) is calculated as follows (18):

$$OEF = 1-Y = \delta\omega \cdot \left(\frac{4}{3}\pi \cdot \gamma \cdot B_0 \cdot Hct \cdot \Delta\chi_0\right)^{-1}. \qquad (1.29)$$

The concentration of deoxyhemoglobin per unit tissue volume is calculated as follows (18):

$$C_{deoxy} = \frac{3}{4} \cdot \frac{\zeta \cdot \delta\omega \cdot n_{Hb}}{\gamma \cdot \pi \cdot \Delta\chi_0 \cdot B_0}, \quad (1.30)$$

where n_{Hb} is the total intracellular Hb concentration equal to $5.5 \times 10^{-6} mol/mL$ (18). Since *Hct* was not measured in GEPCI experiments, we will report only relative regional OEF (OEF_{rel}) values.

$$OEF_{rel} = \delta\omega / \delta\omega_{mean} \quad (1.31)$$

1.4 Summary

In summary, my dissertation primarily uses the following two models:

$$\begin{aligned} S(TE) &= A_0 \cdot \exp\left(-R2^* \cdot (TE + TE_1) + i \cdot 2\pi \cdot \Delta f \cdot (TE - TE_1)\right) \cdot F(TE) \\ S(TE) &= A_0 \cdot \exp\left[-R2t^* \cdot (TE - TE_1) + i \cdot 2\pi \cdot \Delta f \cdot (TE - TE_1)\right] \cdot F_{BOLD}(TE) \cdot F(TE) \end{aligned}, \quad (1.32)$$

where *TE* is the gradient echo time, *R2t*=1/T2t** is the tissue transverse relaxation rate constant (which describes GRE signal decay in the absence of the BOLD effect), Δf is the frequency shift (which depends on tissue structure and on the macroscopic magnetic field, which is created mostly by tissue/air interfaces), function $F_{BOLD}(TE)$ describes GRE signal decay due to the presence of a blood vessel network with deoxygenated blood (veins and the part of capillaries adjacent to veins), and function *F(TE)* describes the effects of macroscopic magnetic-field inhomogeneities.

By fitting the equation to the real and imaginary parts of the complex signal via a nonlinear regression algorithm, we are able to find the six parameters A_0, R2*, R2t*, Δf, ζ , and $\delta\omega$ for each voxel in the brain. Based on the fitting results, we can calculate BOLD-related measurements, including OEF, dCBV, C_{deoxy}, and $R2' = \zeta \cdot \delta\omega$. Examples of transverse MRI images are shown below in Figure [4].

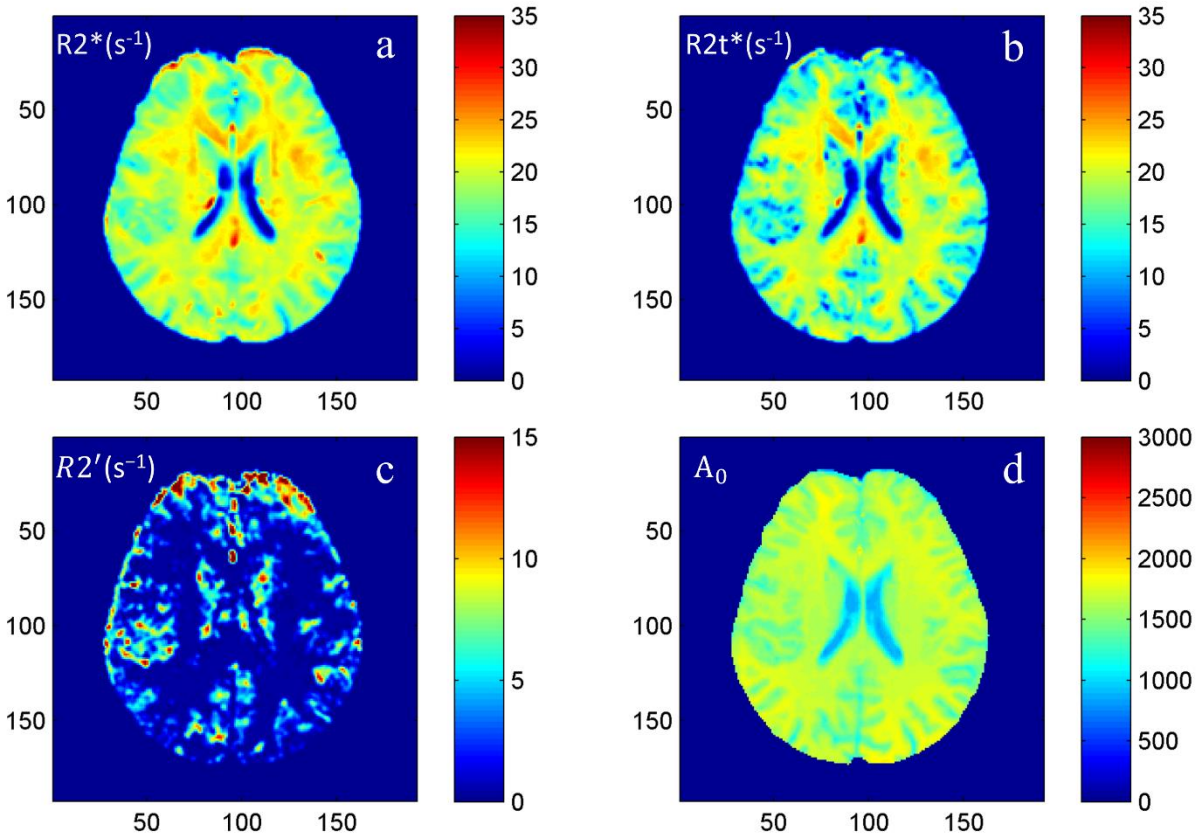

Figure 1.4 Example of transverse GEPCI images computed from the models.

The end of this chapter discusses these similar terms: R2*, R2, and R2t*. Note that, conventionally, in a gradient echo experiment, the total R2* relaxation rate constant is considered a sum of two components: the R2 relaxation rate constant, which represents the part of MR signal decay that cannot be reversed by a refocusing 180° RF pulse; and the $R2'$

relaxation rate constant, which represents the part of the signal decay that can be reversed by a refocusing 180° RF pulse: $R2^{*} = R2 + R2'$. Because GEPCI is based on a gradient echo sequence—although R2t* excludes the BOLD effect due to the blood vessel network—R2t* still includes the reversible component due to the magnetic susceptibility effects that result from the presence of different cellular components. This is the major difference between R2 and R2t*. Furthermore, R2 is usually used to represent the spin-spin interactions in a single compartment model where protons locate in a homogenous environment. However, due to the complicated biological environment, protons may locate in multiple compartments: e.g., protons in myelin layers, protons in axons, and protons in CSF. As a result, the interactions of protons with protons and protons with other biological molecules are not homogenous in the multiple compartment environment. In this circumstance, it is confusing to use R2 to represent all these spin-spin interactions, so this is considered the irreversible part of R2t*. All in all, although R2t* excludes the BOLD effect due to the blood vessel network, it still includes both an irreversible component due to spin-spin interactions (e.g., protons with protons and protons with other molecules) and a reversible component due to the susceptibility effects of biological components.

Chapter 2: Introduction to Normal Aging and Alzheimer's Disease

Alzheimer's disease (AD) affected approximately 48 million people worldwide in 2015. Its devastating consequences have stimulated an intense search for AD prevention and treatment. Although normal aging and Alzheimer's disease can cause similar cognitive deficits and clinical symptoms (e.g., memory loss), the underlying pathological changes are quite different. For decades, it has been commonly believed that normal aging causes significant neuron death in the neocortex and hippocampus. However, modern quantitative studies suggest that neuron number is preserved in normal aging, so neuron death is unlikely to account for the age-related impairment of neocortical and hippocampal functions. With significant brain atrophy and neocortical thinning, one can hypothesize that the neuronal density increases with increasing age, which is also supported by the literature. In contrast, there is considerable evidence for significant neuron loss in the hippocampal area in Alzheimer's disease. Previous studies have also shown that neuronal damage is caused by neurotoxic pathological changes such as amyloid plaques and tau tangles. Therefore, it is necessary to review the qualitative and quantitative pathological changes of normal aging and Alzheimer's disease with respect to neuron loss. Currently, radiotracers and positron emission tomography (PET) imaging are widely used to detect amyloid deposition and tau tangles *in vivo*. But there is also a potential for the GEPCI approach to the *in vivo* detection of these microstructural changes that avoids the disadvantages of PET imaging.

2.1 Normal Aging

2.1.1 Non-significant Age-related Neuron Loss

Although it is well known that normal aging can cause functional cognitive impairments, the neurobiological effects of normal aging (i.e., changes in the cellular content and organizations, including cerebral cortical thinning and atrophy) on functional and structural declines are still not well understood (19). A conventionally accepted idea dating back to the 1950s is that significant neuron death is found both in aged humans without AD and in nonhuman primates and rodents (20, 21). Although the percentage of neuron loss varies in these two studies, they both suggest that most neocortical regions and certain hippocampal subfields lose neurons by 25% to 50% with age. For example, Brody et al. (20) examined 20 brains of individuals between the ages of newborn to 95 years. They report that the cell number decreased with age in all cortical layers. The greatest decrease in cell number with increasing age occurred in the superior temporal gyrus followed by the precentral gyrus and then the area striata. However, the data may be confounded by species and strain differences, tissue processing, and sampling procedure.

Application of stereological procedures to count the neurons of several species, including humans, yielded the surprising result that the number of neurons does not significantly change due to normal aging in the cortex and hippocampus (19). Consider a few studies that support this surprising result. Terry et al. (22) studied 51 brains from clinically and neuropathologically normal individuals ranging in age from 24 to 100 years. They report that the total neuron populations in the mid-frontal, superior temporal, and inferior parietal sections did not decline significantly with age. Furthermore, the total neuron counts in the young group did not differ significantly from those in the old group in the midfrontal cortex or the superior temporal cortex. Only in the inferior parietal area is the difference significant, but the p value is 0.05 at the cut-off

of significance level. Haug and Eggers (23) examined 60 brains and report that the brain volume of frontal cortex significantly decreased but that loss of neurons cannot be found. As a result, the neuronal density increased in the frontal cortex. Furthermore, the size of neurons and the number of synapses decrease with age. Pakkenberg and Gundersen (24) examined 94 brains from a Danish population and report that the average numbers of neocortical neurons are 19 billion in female brains and 23 billion in male brains: a 16% gender difference. A rather small decline (approximately 10%) of neocortical neurons were found over the life span from 20 to 90 years in the human neocortex. However, they warn that, due to the experimental design, this small decline with age should not be considered strong evidence for biologically significant age-related neuron loss. Pakkenberg et al. examined the same 94 brain samples in 2003 (25) and report that the number of glial cells in six elderly individuals with a mean age of 89.2 years was not significantly different from that of six young individuals with a mean age of 26.2 years. Furthermore, the total myelinated fiber length varies from 150,000 to 180,000 km in young individuals and shows a large reduction with age. Freeman et al. (26) examined the cerebral cortex of 27 normal individuals ranging in age from 56 to 103 years. They found that the frontal and temporal neocortical regions exhibited clear evidence of cortical thinning with age but that total neuronal numbers in the frontal and temporal neocortical regions remained relatively constant over a 50-year age range. As a result, frontal and temporal cortical neuronal density showed a small but insignificant increase with increasing age. Freeman et al. also discuss what leads to cortical thinning. The data suggest that loss of neuronal and dendritic architecture, rather than loss of neurons, underlies neocortical volume loss and cortical thinning with increasing age in the absence of AD.

Based on the findings in literature, we can see neuron loss is not significant due to normal aging. In addition to neurons, the number of other CNS cells such as glial cells did not show significant differences between elderly individuals with a mean age of 89 years and young individuals with a mean age of 26 years (25). Furthermore, the glia/neuron ratio of 1.32 for females and 1.49 for males showed no statistically significant correlation with age over adult life (27). Thus, the published studies indicate that the total number of neurons and glial cells in the cortex remains relatively constant over normal adult life.

2.1.2 Age-related Brain Atrophy and Cortical Thinning

Cerebral volume loss and cortical thinning has been observed in various structural MRI studies associated with normal aging. A few studies are cited to support this observation. Scahill et al. (28) scanned 39 healthy control subjects ranging in age from 31 to 84 years. They find a significant decrease in cross-sectional whole brain, temporal lobe, and hippocampal volumes, and a significant increase in ventricular volume with age. Fotenos et al (29) also used structural MRI to scan 370 adults ranging in age of 18 to 97 years. 192 participants were non-demented, while the rest (98 participants) exhibited very mild to mild dementia of the Alzheimer type. They find that both cortical and white-matter volume decrease with age; gray matter volume declines in a linear fashion from early adulthood, whereas white matter volume loss appears to start later in life and does not follow a linear pattern. The onset of dementia is associated with an accelerated atrophy rate.

Thinning of the cerebral cortex over age has also be found in many studies. A few studies are cited here to support this statement. Salat et al. (30) measured the cortical thickness in 106 non-demented participants ranging in age from 18 to 93 years by using a T1-weighted MRI. They find that the global thickness significantly declines with increasing age. In regional measures,

significant thinning was found in the occipital lobe, the pre/post central gyrus, and the inferior lateral prefrontal cortex. Temporal lobe thinning is relatively less significant compared to that observed in other cortical areas. Similarly, our study (Chapter 3) (12) also shows that cortical thickness significantly decreases with age in most of the cortical regions segmented in FreeSurfer. The thinning rate varies across cortical regions of the brain. The 20 participants in this study were healthy controls ranging in age from 22 to 74 years.

2.1.3 Neuronal Density may Increase with Age

The unchanged number of neurons and the decreasing cortical volume imply increasing neuronal density with increasing age in the cortex, which is also supported by the results of Haug and Eggers (23, 31). They performed morphometric analysis of neurons on human brains and measured five Brodmann cortical areas. These areas include, (i) area 6 in the frontal lobe, also designated the supplementary motor area; (ii) area 11 in the orbital part of the frontal lobe, which is linked to psychosocial functions; (iii) area 7 in the parietal lobe, which is related to sensory and speech analysis; (iv) area 17 or the visual cortex in the occipital lobe; and (v) area 20 at the basis of the temporal lobe. The measurements are based on at least 50 brains in each area, except for area 20, for which the measurements of only 20 brains are provided. They find that the neuron density increases significantly with age in areas 6 and 11 in the frontal lobe ($p = 0.01$) and in area 17 in the occipital lobe ($p = 0.001$), while area 7 in the parietal lobe and area 20 in the inferior temporal gyrus show non-significant but increasing tendencies. They also confirm that the total number of neurons in the human cerebral cortex does not change during normal aging. This result may not be representative of brain regions other than the cortex.

As mentioned above, Freeman *et al* (26) also find that frontal and temporal cortical neuronal density shows a small increase with increasing age. Although few studies directly measure

neuronal density over age, the unchanged number of neurons and cortical thinning with age are widely supported by previous studies, which is a strong indications of increased neuronal density.

2.1.4 Age-related Dendritic and Synaptic Loss

But if loss of neurons is not significant in normal aging, what leads to cortical thinning and volume loss? A more recent point of view is that relatively subtle alterations in synaptic connectivity, dendritic spine density, and neural plasticity (32-35) are associated with age–related cognitive dysfunctions. A significant reduction in the dendritic arbors of pyramidal neurons located in the prefrontal, superior temporal, and precentral cortices, and changes in dendritic spine size, shape, and density across the neocortex in humans and animals are discussed by Dickstein (33). Hof and Morrison (34) argue that, while neuron death predominates in Alzheimer's disease, age-related cognitive impairment is probably mediated by changes in synaptic communication rather than by neuron death. Fjell et al. (32) also argue that regions with a high degree of life-long plasticity are more affected by normal aging effects. Freeman et al. (26) argue that previous studies suggest an age-related decrease in neuronal size (13) and a loss of presynaptic terminals (28). A loss of complexity of dendritic arborizations has also been described in Golgi studies of "normal" aging. The reported observation of volume loss in the white matter also suggests that some of the decrease in cortical thickness could be attributed to loss of ascending projections in the cortex. Together, these data suggest that loss of neuropil (i.e., neuronal structural complexity) might contribute to the dramatic thinning that occurs with increasing age.

In summary, much evidence shows that neuron loss is not significant over the normal aging process, while cerebral atrophy and thinning are significant. Thus, neuronal density should

significantly increase with age. However, most of the studies cited that are related to neuronal structure were conducted on non-human primates or other animals or on post-mortem human tissues. Hence, it is essential to study the age-related cellular and functional alterations quantitatively *in vivo* and to establish a baseline for distinguishing normal aging from pathological effects.

2.2 Alzheimer's Disease

2.2.1 A Staging Model of Alzheimer's Disease

Over the past two to three decades, a staging model of Alzheimer's disease (AD) has been developed. Both AD pathological processes and clinical decline progress gradually. Pathological changes begin to develop decades before the earliest clinical symptoms occur. Dementia occurs at the last stage of many years of accumulation of these pathological changes. At present, the clinical diagnosis of AD requires the presence of dementia.

The clinical disease stages of AD have been divided into three stages (36). The first is referred to as a pre-clinical stage in which individuals are cognitively normal but have AD pathological changes. Notice that some of these individuals die without ever showing AD clinical symptoms. The hypothesis is that an asymptomatic individual with AD-related pathological changes would ultimately have become symptomatic if he or she lived long enough. The second is commonly referred to as mild cognitive impairment (MCI), in which the earliest cognitive symptoms (typically deficits in episodic memory) occur but do not meet the criteria for dementia. The severity of cognitive impairment in the MCI stage varies from the earliest appearance of memory loss to more widespread dysfunction in other cognitive domains. The final phase in the evolution

of AD is dementia, in which impairments in multiple domains are severe enough to produce cognitive deficits.

Dementia is the clinically observable result of the cumulative burden of AD pathological changes in the brain. A clinical diagnosis of dementia indicates that the patient has a disorder that precludes independent living and is on an inevitable course toward complete loss of independence. Most elderly patients with dementia have multiple pathological changes underlying their dementia. AD is the most common pathological substrate, which is referred to as dementia of the Alzheimer type (DAT).

To date, all disease-modifying experimental therapies for AD have failed to demonstrate a clinical benefit in individuals with symptomatic AD (37, 38), possibly because the drugs were administered too late in the course of the disease, which begins 15-20 years prior to the onset of clinical symptoms (36, 39-45). As a result, the preclinical stage is an important time window for therapeutic intervention. Hence, one of the important directions in AD therapy is to develop widely accessible neuroimaging techniques that can detect AD brain pathology in the preclinical stages. Many biomarkers have been developed to detect pathological changes in the preclinical stage and to identify individuals who are destined to develop AD in the early disease course. Herein, several hallmark AD pathological changes and widely used biomarkers are introduced briefly.

2.2.2 Amyloid Deposition

One of the prevailing hypotheses of AD is the amyloid cascade hypothesis (36, 39, 41, 42), which suggests that abnormal accumulation of (Aβ) in the neocortex is one of the earliest pathological markers of AD. Aβ deposition is actually the product of a larger transmembrane

protein: the amyloid precursor protein (APP) (46). The abnormal metabolism of APP leads to excess production or reduced clearance of Aβ in the cortex.

Both CSF $A\beta_{42}$ and radiotracers of amyloid PET imaging are biomarkers of Aβ deposition. Klunk et al. (47) report the first human study of a novel amyloid PET imaging tracer—Pittsburgh Compound-B (PiB)—in 16 patients with diagnosed mild AD and 9 controls. The retention of PiB measured by PET imaging (PiB PET) *in vivo* reveals a large amount of amyloid deposits in cerebral cortical areas of the AD brains, especially in the prefrontal cortex and precuneus (47, 48). PiB retention was equivalent in both AD patients and controls in areas known to be relatively unaffected by amyloid deposition (such as subcortical white matter, pons, and cerebellum). Studies in three young (21 years) and six older healthy controls (69.5 ± 11 years) showed low PiB retention in cortical areas and no significant group differences between young and older controls. Later on, Ikonomovic et al. (49) examined patients who underwent PiB PET imaging before death and autopsy. They report a strong direct correlation between PiB retentions *in vivo* and region-matched quantitative measures of amyloid plaques of the AD subjects. They also find that PiB binds specifically to fibrillary Aβ and not to soluble Aβ or diffuse Aβ plaques. This study further supports the validity of PiB-PET imaging as a method for *in vivo* evaluation of Aβ plaque burden.

Low concentrations of CSF $A\beta_{42}$ correlate with both the clinical diagnosis of AD and with Aβ neuropathology at autopsy. An inverse relation has been reported between *in vivo* PiB amyloid imaging and CSF $A\beta_{42}$ in AD patients who have undergone both tests (50). The evidence therefore strongly supports the hypothesis that both amyloid imaging and low CSF $A\beta_{42}$ are valid biomarkers of brain Aβ-plaque load.

However, amyloid deposition has been shown to start while individuals are still cognitively normal. It is hypothesized that, after an early phase of fast accumulation, a plateau is reached by the time of cognitive decline (36). In the study by Villain et al. (51), 32 patients with AD, 49 subjects with MCI, and 103 healthy controls underwent two PiB PET scans 18 months apart. They report no significant association between the PiB retention rate of change and the clinical status or disease progression. Amyloid accumulation seems to slow down at the latest stages of the process.

2.2.3 Neurofibrillary Tau Tangles

So amyloid deposition is not related to clinical symptoms as closely as another hallmark abnormal protein deposit: neurofibrillary tangles (NFTs) formed by hyperphosphorylated tau. Bennett et al. (52) examined 44 individuals with clinically diagnosed AD and 53 without dementia with a uniform structured clinical evaluation for AD and cognitive testing about 8 months prior to death, and brain autopsy at death. They report that, when a term for tau tangles is added to the multiple regression model with amyloid, the association of amyloid load with clinical disease or global cognitive tests is reduced by more than 60% and is no longer significant, whereas the association of tangles with clinical disease is essentially unchanged. Giannakopoulos et al. (53) examined 22 elderly cases with clinical dementia assessment (MMSE), stereological assessment of NFT, unaffected neurons, and total amyloid volume in the CA1 field of the hippocampus, entorhinal cortex, and Brodmann area 9 (frontal area). Multivariate analyses show that total NFT counts in the entorhinal cortex and area 9 as well as neuron numbers in the CA1 field are the best predictors of the MMSE score. The amyloid volume has no additional predictive value, in terms of clinicopathologic correlations, beyond its interaction with NFT.

However, the prior lack of imaging agents has limited studies of tau to postmortem examinations or measures that lack topographic information such as measurement of tau in CSF. A recent study by Brier et al. (54) reports PET imaging of tau and Aβ in a cohort of cognitively normal older adults and older adults with mild AD. They also discuss the fact that tau deposition in the temporal lobe more closely tracks dementia status and is a better predictor of cognitive performance than Aβ deposition in any region of the brain.

2.2.4 Neuron Loss in the Hippocampal Area

However, an autopsy study has confirmed that gross cerebral atrophy (indicating the loss of synapses and neurons), and not Aβ or NFT burden, is the most proximate pathological substrate of cognitive impairment in AD. For example, Savva et al. (55) assessed 456 brains from people 69 to 103 years of age at death. They report that the associations between dementia and pathological changes (amyloid deposition and tau tangles) attenuate with increasing age. In contrast, atrophy of the hippocampus and the neocortex is strongly associated with dementia at all ages.

Based on the above discussions, Aβ abnormalities precede tau abnormalities and NFTs precede cerebral atrophy. Additionally, patterns of gray matter loss are associated with NFT pathology at Braak stages V and VI (56). 83 subjects with Braak stage III through VI underwent ante-mortem and post-mortem AD staging. The Braak stage V and VI groups showed a pattern of gray-matter loss affecting the medial temporal lobes (MTL), including the hippocampus, the entorhinal cortex, and the adjacent parahippocampal gyrus, which is vulnerable to NFTs. Subjects with a high tau burden showed a pattern of gray-matter loss affecting the hippocampus, parahippocampal gyrus, and lateral temporal lobes compared with subjects with a low tau burden.

Indeed, the medial temporal lobe is an essential area related to human memory and to AD. Reduction of volume and loss of cells in the entorhinal cortex and hippocampus have been extensively reported in participants with mild cognitive impairment (MCI) and AD (57-61). For example, Price et al. (59) examined the neuron number and volume in the entorhinal cortex and CA1 field of the hippocampus from 4 groups of participants, including 13 non-demented cases with healthy brains, 4 cases with preclinical AD, 8 cases with very mild symptomatic AD, and 4 cases with severe AD. They report no significant decrease in neuron number or volume with age in the healthy non-demented group and little or none in the healthy and preclinical AD groups. They report substantial decreases in neuron number and volume in the very mild AD group. Greater damage was observed in CA1 in the severe AD group. The results indicate that symptomatic AD begins only when neuron loss occurs in the hippocampal area, which is consistent with the study by West et al (62).

The posterior parahippocampal gyrus draws relatively less attention, but several studies have reported its atrophy due to aging (63) and AD (64). The presence of neurofibrillary tangles (NFTs) and neuronal loss in the parahippocampal gyrus—previously reported by Thangavel *et al* (65)—can also affect R2* measurements. However, their participants were assessed at death after nearly a decade of dementia. In addition, tissue damage in the parahippocampal gyrus was smaller than that in the hippocampus (66).

2.2.5 Clinical Dementia Rating (CDR)

The above sections introduce hallmark AD pathological features. This section introduces a clinical evaluation for identifying cognitive impairment. This evaluation, referred to as clinical dementia rating (CDR), has been developed by Washington University. The CDR is a 5-point scale used to characterize six domains of cognitive and functional performance applicable to

Alzheimer disease and related dementias: memory, orientation, judgement & problem solving, community affairs, home & hobbies, and personal care. The necessary information to make each rating is obtained through a semi-structured interview of the patient and a reliable informant or collateral source (e.g., a family member). The score is useful for characterizing and tracking a patient's level of impairment/dementia:

0 = Normal

0.5 = Very Mild Dementia

1 = Mild Dementia

2 = Moderate Dementia

3 = Severe Dementia

The scoring rule is to use all of the information available and to make the best judgement. Score each category (M, O, JPS, CA, HH, PC) as independently as possible. Mark in only one box for each category, rating impairment as a decline from the person's usual level due to cognitive loss alone, not impairment due to other factors, such as physical handicap or depression. Occasionally the evidence is ambiguous and the clinician's best judgment is that a category could be rated in either one of two adjacent boxes, such as mild (CDR=1) or moderate (CDR=2) impairment. In this situation, the standard procedure is to check the box of greater impairment. The derivation of the global CDR from the scores in each of the six categories is described in detail by Morris (67).

2.3 MRI Application in Microstructural Changes

As mentioned above, PET imaging is widely used to measure the retentions of biomarkers of amyloid and tau deposition in AD studies. But MRI is widely available worldwide, is non-invasive ,and does not require radiation exposure. For both normal aging and AD, a structural MRI can provide accurate volume measurements as post-mortem measurements. For example, Bobinski et al. (68) examined 11 AD cases and 4 healthy controls and measured the post-mortem volumes of the hippocampal subdivisions by using MRI and histological sections. They report strong correlations between these two measurements, which indicate that an accurate volumetric measurement of the hippocampus can be obtained via MRI. However, atrophy occurs at a later stage of the AD process, so structural MRI cannot effectively give an early diagnosis for the preclinical stage. Furthermore, the volumetric measurements lack biological information, so a quantitative MRI technique is needed to identify early AD pathological changes and to provide biological information at a microstructural level.

This is possible because all of the AD pathological processes that contribute to the pathogenesis of Alzheimer's disease at the cellular level lead to changes in the environment of local tissue water molecules – a major source of MRI signal. Hence, in addition to measuring brain atrophy by using volumetric MRI, a properly designed MRI technique can enable local water molecules to report on regional biological tissue properties at the cellular level.

The GEPCI approach could be a potential candidate for this motivation. The GEPCI approach has been used to identify brain tissue damage in multiple sclerosis (2, 4, 69-72) and psychiatric diseases (73). R2* values have been found to be significantly lower in patients with multiple sclerosis (MS) than in healthy participants (2, 4, 69-72). Significant correlations between age-adjusted R2* measurements and clinical scores of MS have also been reported for cortical regions (71). Significant group effects based on GEPCI measurements have been observed in the

superior temporal cortex and in the thalamus in participants with schizophrenia and bipolar disorder Because GEPCI metrics (R2* and R2t*) are sensitive to the tissue-water environment in the human brain, the measurements can be very hard to interpret. As a result, GEPCI is first applied to study healthy controls with normal aging, (i) to establish an age-related baseline, and (ii) to gain a better understanding of the biological interpretation of GEPCI metrics (12). GEPCI is then utilized to detect the pathological changes of the preclinical and the early Alzheimer disease *in vivo* (74).

Chapter 3: On the Relationship between Cellular and Hemodynamic Properties of the Human Brain Cortex Throughout Adult Lifespan

3.1 Introduction

Establishing baseline MRI biomarkers for normal brain aging is significant and valuable for separating normal aging effects from neurological diseases. In this study, for the first time we have simultaneously measured a variety of tissue specific GEPCI metrics of healthy adults (ages 22 to 74 years), such as T1-wegihted, R2*, R2t*, OEF, dCBV and C_{deoxy}. GEPCI metrics are utilized to establish quantitative in vivo biomarkers characterizing the age-related evolution of tissue structural and functional properties of adults. Two main goals of this study are: **(i)** to investigate the age-related changes of GEPCI metrics so a baseline for normal aging can be established; **(ii)** based on GEPCI age-related results and what we know about the pathology of normal aging from the literature (reviewed in Chapter 2), find out a proper biological interpretation for GEPCI metrics, especially R2* and R2t*. Both the age-related baseline and the biological interpretation of GEPCI metrics are essential for us to investigate diseases in the future.

The data (20 healthy subjects) show that in most cortical regions R2t* increases with age while tissue hemodynamic parameters, i.e., relative oxygen extraction fraction (OEF_{rel}), deoxygenated

cerebral blood volume (dCBV) and tissue concentration of deoxyhemoglobin (C_{deoxy}) remain practically constant. R2t* describes the part of the signal decay resulting from water molecule interactions with cellular and extracellular components of biological tissues. By comparing our results with the literature data, we hypothesize that in the normal brain it can serve as a biomarker of the cortical "cellular packing density" – a parameter mostly proportional to the number of neurons and glia cells in the unit tissue volume – and can potentially identify tissue alterations (see further comments in the Discussion section). We also use this hypothesis to explain the relationships between R2t* and the functional data (e.g., OEF). Specifically, thicker cortical regions have lower R2t* and these regions have lower OEF.

The baseline GEPCI-based biomarkers obtained herein could also serve to help distinguish age-related changes in brain cellular and hemodynamic properties from changes which occur due to neurodegenerative diseases, e.g., (71).

3.2 Methods

3.2.1 Participants

This study was approved by the Institutional Review Board of Washington University School of Medicine. Twenty participants aging from 22 to 74, including 7 male (ages: 22, 26, 29, 35, 37, 42, 65) and 13 female (ages: 23, 28, 33, 42, 45, 46, 50, 52, 56, 57, 61, 61, 74), were recruited in this study. None of the participants had any history of neurological diseases. All participants provided informed consent.

3.2.2 Data Acquisition

All subjects were scanned in a 3T Trio MRI scanner (Siemens, Erlangen, Germany). A 3D multi gradient echo sequence was used to obtain the data. Sequence parameters were: resolution 1×1×2 mm^3 (read, phase, slab), FOV 256 mm×192 mm, repetition time TR = 50ms, flip angle 30°, 10 gradient echoes with first gradient echo time TE_1 = 4 ms, echo spacing ΔTE = 4ms. Additional phase stabilization echo (the navigator data) was collected for each line in k-space to correct for image artifacts due to the physiological fluctuations (4). The total acquisition time of GEPCI is 11 mins 30s. Field inhomogeneity effects were removed by using the voxel spread function (VSF) approach (3). Standard clinical Magnetization-Prepared Rapid Gradient Echo (MPRAGE) (75) images with TR/TI/TE = 2200/1100/3.37 ms and the resolution 0.9×0.9×1.5 mm^3 were also collected for segmentation purposes. The total acquisition time of MPRAGE is 6 mins. After the data acquisition, the raw k-space data were read into MATLAB (The MathWorks, Inc.) for the post-processing.

3.2.3 Data Analysis and Image Generation

The image processing was finished in MATLAB (The MathWorks, Inc.) using models described in Chapter 1:

$$\begin{aligned} S(TE) &= A_0 \cdot \exp\left(-R2^* \cdot (TE + TE_1) + i \cdot 2\pi \cdot \Delta f \cdot (TE - TE_1)\right) \cdot F(TE) \\ S(TE) &= A_0 \cdot \exp\left[-R2t^* \cdot (TE - TE_1) + i \cdot 2\pi \cdot \Delta f \cdot (TE - TE_1)\right] \cdot F_{BOLD}(TE) \cdot F(TE) \end{aligned} \quad (3.1)$$

where TE is the gradient echo time, R2* is the global transverse relaxation rate constant, R2t*=1/T2t* is the tissue transverse relaxation rate constant in the absence of BOLD effect, Δf is the frequency shift (dependent on tissue structure and also macroscopic magnetic field created mostly by tissue/air interfaces), function $F_{BOLD}(TE)$ describes GRE signal decay due to the presence of blood vessel network with deoxygenated blood (veins and the part of capillaries

adjacent to veins), and function F(TE) describes the effects of macroscopic magnetic field inhomogeneities.

As mentioned in Chapter 1, by fitting the equation to the real and imaginary parts of the complex signal using nonlinear regression algorithm, six parameters are computed: A_0 (T1-weighted), R2*, R2t*, Δf, ζ and $\delta\omega$ for each voxel in the brain. ζ and $\delta\omega$ are computed from $F_{BOLD}(TE)$. Based on the fitting results, BOLD-related measurements are computed, including OEF, dCBV, and C_{deoxy}.

In this study, the relative regional OEF (OEF_{rel}) is reported as:

$$OEF_{rel} = \delta\omega / \delta\omega_{mean} \tag{3.2}$$

where $\delta\omega_{mean}$ is the mean across the cerebral cortex and $\delta\omega$ represents one single cortical region.

3.2.4 Image Segmentation

MPRAGE images were input into FreeSurfer (Laboratory for Computational Neuroimaging, Martinos Center for Biomedical Imaging) (76) to generate brain segmentations and calculate cortical thickness. 26 cortical regions of interest (ROI), covering frontal, temporal, parietal and occipital lobes, were chosen to characterize an individual participant's cortex. The thalamus, caudate, putamen, pallidum, hippocampus and amygdala were chosen to study the subcortical regions.

MPRAGE images were registered to GEPCI-T1-weighted images using FMRIB's (Functional Magnetic Resonance Imaging of the Brain) Linear Image Registration Tool (77, 78) in FMRIB Software Library (FSL) and the transformation matrices of the registration were computed. Finally, these matrices were applied to the brain segmentations from FreeSurfer and transformed

them to the space of GEPCI-T1-weighted images. Since GEPCI –T1-weighted images are naturally co-registered with all GEPCI maps (R2*,R2t*, OEF_{rel}, C_{deoxy}, and dCBV), the segmentations were also naturally registered to all these maps.

Even though the data were collected with rather high in-plane resolution – 1x1 mm^2, they are still susceptible to the partial volume effect (edge values, outliers). To minimize it, a CSF mask generated from FSL is applied further removing CSF signals from FreeSurfer segmentations. Furthermore, in each of the FreeSurfer ROIs which usually contains thousands of voxels, the median of the corresponding measurement distribution was computed because it is less sensitive to outliers. This procedure also minimizes the errors in the model parameters estimates discussed in 3.2.6 Error analysis.

3.2.5 Image Segmentation

The correlations and linear regressions were established using the LinearModel class in MATLAB (The MathWorks, Inc.). As mentioned above, for each GEPCI parameter, the median value was calculated across thousands of voxels within each Freesurfer ROI. As a result, an individual participant has 7 parameters (R2*, R2t*, OEF_{rel}, dCBV, C_{deoxy}, cortical thickness (Th), and SR2t*=R2t*×Th) and 26 median values from the cortical ROIs for each parameter. So for each parameter and each ROI, the following equation is used to calculate a correlation and linear regression between the parameter and age across 20 participants:

$$parameter_{ROI} = a_{ROI} + k_{ROI} \cdot (age - 40) \tag{3.3}$$

Age 40 years was selected arbitrarily as the adult reference age for the convenient interpretation of the intercept a_{ROI}. Then a_{ROI} represents the characteristic value of a parameter within a ROI

taking into account all 20 participants. a_{ROI} corresponds to an averaged 40-year old adult. There are 26 a_{ROI} and k_{ROI} for each parameter across the cortical ROIs. To visualize the distribution of the parameters across 26 cortical ROIs, a_{ROI} can be mapped onto the Freesurfer brain surface. a_{ROI} is used to investigate the relationship between parameters across 26 cortical ROIs. If the parameter doesn't have a significant linear relationship with age, the characteristic value of the parameter within a ROI is just the average across all the participants. The p-values were calculated to evaluate each correlation and conventionally $p < 0.05$ is considered as a significant correlation. Multiple comparison analysis was not applied here because we only reported individual correlations instead of comparing them across different ROIs.

3.2.6 Error Analysis

The simulated data were generated to test the accuracy of the theoretical model, Equation (3.1), used in this study. As the frequency (Δf) has minimal effects on the fitting process, only the amplitude of the signals were used in this simulation. First, the true values of the parameters were assigned based on our typical results: R2t* = 17, OEF = 40%, and dCBV = 3%. Then the parameters were substituted into Equation (3.1) to generate the "true" signals over 10 TEs from 4ms to 40ms. Second, a set of "real" signals over 10 TEs was generated by adding the random noise to the true signals. A typical SNR in GEPCI experiments is between 300 and 500 (for Hanning filtered data). In the simulated data, the noise corresponding to SNR equal to 400 is used. The random noise values were drawn from the standard normal distribution generated by a built-in function in MATLAB. In total, 500,000 sets of the simulated signals were generated in this way. Third, the same fitting routine was applied to each set of the simulated signals to

calculate the output parameters. Finally, the medians, means and standard deviations of each parameter were calculated.

3.3 Results

3.3.1 Age-related Changes in the Cerebral Cortex

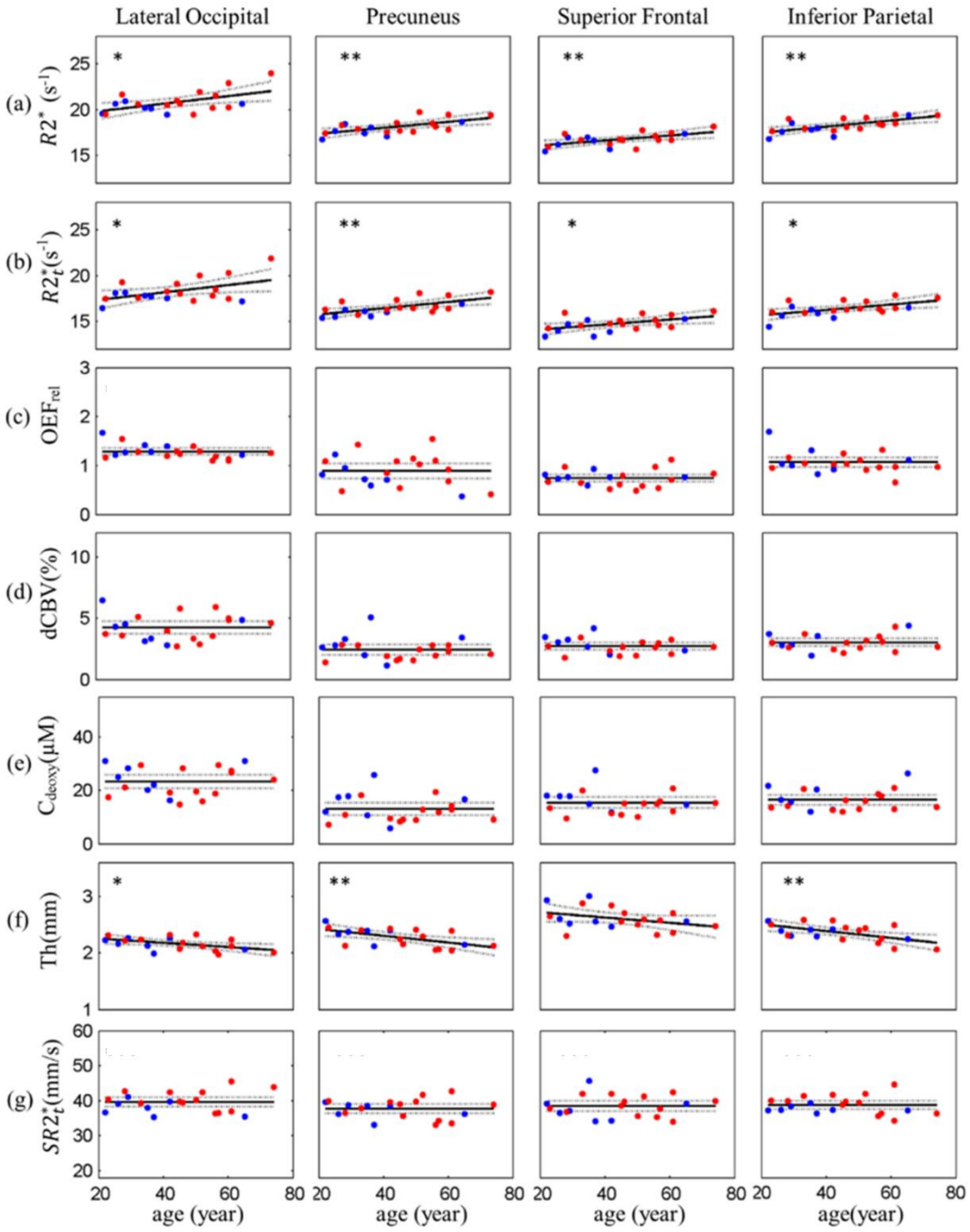

Figure 3.1 Examples of the scatter plots of (a) R2*, (b) R2t*, (c) OEF_{rel} (local-to-global ratios, Eq. [2]), (d) dCBV, (e) C_{deoxy}, (f) cortical thickness (Th) and (g) SR2t* versus age are shown in 4 selected cortical ROIs. Each plot represents the data from a single cortical region and each point in the plot represents a single participant. Male subjects are represented by blue points and female subjects by red points. For R2*, R2t* and cortical thickness, the solid lines are the regression curves and the p values evaluate the significance of the linear model. SR2t*, OEF_{rel}, dCBV and C_{deoxy} show no significant change with age and are represented by a constant model (the solid lines). The dashed lines in all plots represent the 95% confidence intervals. Number of asterisks or "stars" show significance level: $p < 0.01$ (**), $p < 0.05$ (*). The results of regression analysis from all other regions are listed in Table 3.1 and Table 3.2.

The data (Figures 3.1 and 3.2, Tables 3.1 and 3.2) show that in most cortical regions R2* and R2t* increase with age, OEF_{rel}, dCBV and C_{deoxy} remain constant while cortical thickness, Th, decreases. In addition to parameters listed above, we have also introduced a parameter SR2t* that represents an integrated characteristic of R2t* under a unit square of the cortex and is computed as a product of the median R2t* and Th for each FreeSurfer region: $SR2t^* = R2t^* \times Th$. The detailed role of this parameter will be addressed in the Discussion section.

Figure 3.1a shows that R2* statistically significantly increased ($p < 0.05$) with age in the example cortical ROIs. Furthermore, 21 out of 26 regions listed in Table 3.1 demonstrated that R2* significant increase over age with varying rates (slopes). Although a few regions showed non-significant results, all slopes were positive demonstrating an increasing trend of R2* over age.

Figure 3.1b shows that R2t* also significantly increased ($p < 0.05$) with age in the example ROIs. Furthermore, 15 out of 26 regions listed in Table 1 showed significant increase over age with varying rates (slopes). In general, p values for R2t* regression are higher than those for R2* regressions. As a result, a few regions with significant increases in R2* showed non-significant increases in R2t*. For example, in the insula cortex, R2* significantly increased with age (p =

0.020) while R2t* did not (p = 0.14). Again, all slopes were positive. So although some regions didn't have significant results, there was always an increasing trend of R2t* over age.

Figure 3.1c shows that the relative OEF (OEF_{rel}, a local-to-global ratio, Equation (3.2)), showed no significant trend with age – the p values of the linear model were not significant ($p > 0.05$) in all cortical regions except the rostral-middle frontal ($p= 0.013$) and the lateral occipital ($p= 0.026$). To describe this data, a constant model is used in all cortical regions. The mean values of OEF_{rel} are shown in Figure 3.1 as solid lines with the 95% confidence intervals shown as dashed lines. The mean values and standard deviation were listed in Table 3.2. The mean values of OEF_{rel} ranged from 0.6 to 1.5 across the selected 26 ROIs. The regions in occipital lobe, such as cuneus, lingual and lateral occipital, have comparatively higher OEF_{rel} (Table 3.2).

Results for dCBV (Figure 3.1d and Table 3.2) and C_{deoxy} (Figure 3.1e and Table 3.2) showed similar properties as $OEF_{rel.}$ They have no statistically significant linear trend over age. As a result, a constant model was used for them. The mean values and standard deviation were listed in Table 3.2.

Figure 3.1f shows that cortical thickness significantly decreased ($p<0.05$) with age in the example regions except in superior frontal ($p=0.11$). Furthermore, 17 out of 26 regions listed in Table 3.1 showed significant cortical thinning over age with varying rates (slopes, mm/year). But all slopes are negative, which indicate age-related thinning varied in different regions of the brain.

Results for the integrated parameter SR2t* were analyzed using the same procedure as OEF_{rel} and showed no significant linear relationships with age. They were presented using a constant model demonstrating no significant changes over the studied human lifespans for each ROI

except caudal anterior cingulate (Figure 3.1g). The mean and standard deviation were listed in Table 3.2.

Table 3.1

ROI	R2*			R2		
name	slope	intercept	pvalue	slope	intercept	pvalue
banksst	0.029	18.6	0.020	0.028	16.5	0.021
caudal-anterior cingulate	0.031	15.6	0.011	0.052	13.5	0.004
caudal-middle-frontal	0.034	17.6	0.006	0.021	15.8	0.120
cuneus	0.040	19.7	0.005	0.043	17.8	0.007
fusiform	0.034	18.9	0.007	0.023	16.4	0.093
inferior parietal	0.034	18.2	0.002	0.029	16.3	0.012
isthmus cingulate	0.038	18.3	0.003	0.044	17.2	0.001
lateral occipital	0.041	20.6	0.015	0.040	18.1	0.032
lingual	0.048	19.9	0.005	0.051	18.3	0.009
middle temporal	0.037	18.5	0.002	0.030	14.8	0.060
parahippocampal	0.031	17.2	0.055	0.004	15.0	0.841
paracentral	0.043	19.0	0.001	0.039	17.6	0.027
parsopercularis	0.042	17.0	0.001	0.042	14.8	0.005
parsorbitalis	0.024	18.9	0.106	0.006	15.1	0.699
parstriangularis	0.033	17.6	0.010	0.019	15.0	0.392
postcentral	0.030	18.3	0.005	0.032	16.2	0.017
posterior cingulate	0.029	16.6	0.003	0.028	15.2	0.015
precentral	0.037	18.4	0.003	0.032	16.5	0.020
precuneus	0.033	18.0	0.004	0.034	16.4	0.003
rostral-anterior cingulate	0.014	15.6	0.227	0.006	11.9	0.762
rostral-middle-frontal	0.020	17.1	0.074	0.011	14.8	0.417
superior frontal	0.027	16.6	0.008	0.027	14.7	0.021
superior parietal	0.023	18.3	0.072	0.021	16.1	0.197
superior temporal	0.038	17.6	0.002	0.017	14.4	0.275
supramarginal	0.033	17.6	0.001	0.028	15.5	0.020
insula	0.022	15.5	0.036	0.020	12.5	0.143

Table 3.1 continues on the next page

Table 3.1 (continue)			
ROI	Thickness		
name	slope	intercept	pvalue
banksst	-0.0095	2.51	0.001
caudal-anterior cingulate	-0.0018	2.52	0.617
caudal-middle-frontal	-0.0052	2.49	0.020
cuneus	-0.0035	1.78	0.112
fusiform	-0.0064	2.72	0.002
inferior parietal	-0.0060	2.39	0.007
isthmus cingulate	-0.0030	2.36	0.347
lateral occipital	-0.0038	2.18	0.023
lingual	-0.0043	2.00	0.022
middle temporal	-0.0082	2.86	0.007
parahippocampal	-0.0081	2.69	0.036
paracentral	-0.0050	2.36	0.072
parsopercularis	-0.0081	2.51	0.001
parsorbitalis	-0.0039	2.62	0.228
parstriangularis	-0.0053	2.36	0.028
postcentral	-0.0046	2.03	0.014
posterior cingulate	-0.0055	2.45	0.016
precentral	-0.0064	2.51	0.021
precuneus	-0.0060	2.31	0.009
rostral-anterior cingulate	-0.0040	2.76	0.212
rostral-middle-frontal	-0.0031	2.23	0.168
superior frontal	-0.0047	2.63	0.115
superior parietal	-0.0040	2.12	0.094
superior temporal	-0.0074	2.77	0.008
supramarginal	-0.0073	2.53	0.001
insula	-0.0051	3.02	0.002

Table 3.1: The parameters of Equation 3.3 and p-values for R2*, R2t*, and cortical thickness in 26 selected FreeSurfer ROIs across 20 healthy subjects.

Table 3.2								
ROI	OEF_{rel}		dCBV(%)		C_{deoxy} (μM)		SR2t*(mm/s)	
name	mean	std	mean	std	mean	std	mean	std
banksst	1.14	0.30	3.23	1.22	18.2	6.0	41.0	3.2
caudal-anterior cingulate	0.87	0.54	2.79	1.99	15.2	10.2	34.3	3.4
caudal-middle-frontal	1.02	0.20	2.65	0.53	15.5	3.9	39.1	2.7
cuneus	1.10	0.31	2.70	1.69	14.4	8.5	31.9	3.4
fusiform	1.29	0.21	3.36	1.08	21.0	5.2	44.4	2.8
inferior parietal	1.07	0.22	3.03	0.68	16.5	4.0	38.7	2.5
isthmus cingulate	1.02	0.35	1.18	0.90	6.7	4.5	40.7	3.8
lateral occipital	1.29	0.14	4.25	1.10	23.4	5.4	39.6	2.9
lingual	1.43	0.42	1.88	1.41	10.5	6.5	36.6	2.8
middle temporal	1.05	0.29	6.45	1.59	37.8	9.0	42.1	3.0
parahippocampal	0.99	0.46	1.86	1.41	12.3	8.5	39.8	4.8
paracentral	1.52	0.52	1.12	0.99	8.1	6.6	41.5	4.3
parsopercularis	0.98	0.39	3.09	1.29	17.7	6.1	37.1	2.7
parsorbitalis	1.13	0.49	6.12	1.98	36.2	9.3	39.5	3.4
parstriangularis	0.87	0.36	4.48	2.29	25.1	11.2	35.2	3.9
postcentral	1.21	0.18	2.43	0.88	15.1	5.7	32.9	2.7
posterior cingulate	0.75	0.30	1.88	0.99	10.1	5.5	37.1	2.3
precentral	1.21	0.17	2.21	0.69	13.7	4.7	41.3	3.4
precuneus	0.89	0.33	2.44	0.89	13.0	5.0	37.7	2.8
rostral-anterior cingulate	0.60	0.17	6.25	2.36	34.3	11.1	32.9	5.0
rostral-middle-frontal	0.63	0.20	4.16	1.36	20.9	4.9	33.0	2.7
superior frontal	0.75	0.17	2.74	0.62	15.5	4.3	38.5	3.2
superior parietal	1.25	0.28	2.80	0.74	16.9	5.6	34.2	3.7
superior temporal	0.72	0.22	5.17	1.33	29.1	6.7	39.5	3.8
supramarginal	0.89	0.20	3.23	0.94	17.6	5.1	39.0	2.7
insula	0.60	0.22	3.46	1.04	20.7	6.0	37.8	2.7

Table 3.2: The mean values and standard deviations of the OEF, dCBV, C_{deoxy}, and SR2t* in 26 selected FreeSurfer ROIs across 20 healthy subject.

3.3.2 The Distribution of Parameters on the Brain Surfaces

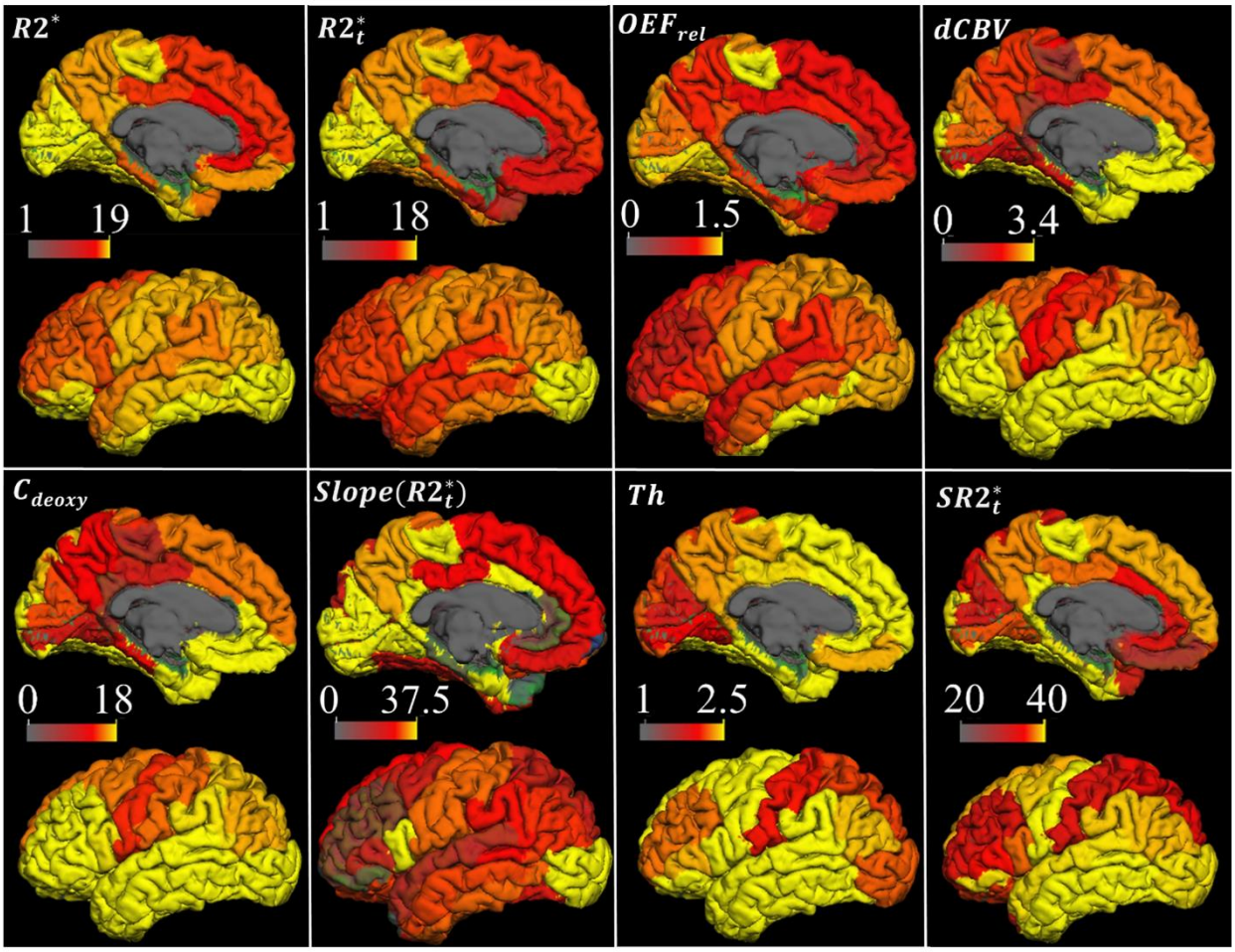

Figure 3.2 The distributions of all GEPCI-derived parameters are presented on the lateral and medial cortical surfaces of the left hemisphere, including R2* (s^{-1}), R2t* (s^{-1}), OEF_{rel}, dCBV(%), C_{deoxy} (μM), cortical thickness (Th) (mm), SR2t* (mm/s), and the regression slope (k_{ROI} from Equation (3.3)) of R2t* vs. age (s^{-1}/year). Images for R2*, R2t*, and Th use the regional characteristic values a_{ROI} from Equation (3.3). Images for SR2t*, OEF_{rel}, dCBV and C_{deoxy} use the regional mean values averaged across all subjects (Table 3.1) because they don't have a significant linear relationship with age. The surface of the cortex was generated by the FreeSurfer at the depth of 0.5 (the voxels in the center of gray matter were sampled). White matter, deep grey matter and ventricles were excluded.

The distributions of all the GEPCI-derived parameters is presented on the lateral and medial cortical surfaces of the left hemisphere in Figure 3.2. Images for R2*, R2t*, and Th use the regional characteristic values a_{ROI} from Equation 3.3. Images for SR2t*, OEF_{rel}, dCBV and C_{deoxy} use the regional mean values averaged across all subjects (Table 3.1) because they don't have a significant linear relationship with age. The ventricles, white matter and deep gray matter are excluded. R2* and R2t* have a similar distributed network. Frontal lobe, inferior parietal, precuneus and posterior cingulate have relatively lower values than paracentral lobule, lateral occipital, cuneus and lingual. This distribution feature is consistent with the previously reported T2* mapping at 7 T resulting from the averaging of 14 subjects (79).

3.3.3 Correlations between Structural and Hemodynamic Cortical Tissue Properties

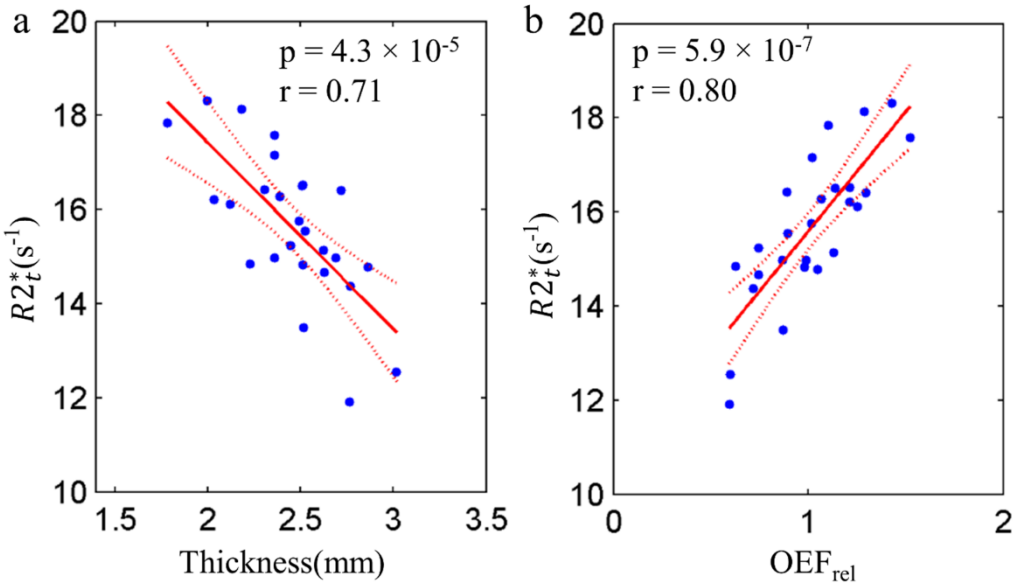

Figure 3.3 The correlation and linear regression of (a) R2t* versus cortical thickness; (b) R2t* versus OEF_{rel}; Each point represents the characteristic value of each FreeSurfer ROIs. The regional characteristic values of R2t* and thickness correspond to a_{ROI} from Equation (3.3). Since OEF_{rel} remains constant with age in the cortical regions, the characteristic values of OEF_{rel} are just the mean values across the subjects in the corresponding regions. All the coefficients from the linear regressions are listed in Table 3.3

Table 3.3				
	slope	intercept	p value	r
R2t* (s^{-1}) vs. Thickness (mm)	-3.96	25.3	4.34E-05	0.71
R2t* (s^{-1}) vs. OEF	5.09	10.5	6.94E-07	0.8

Table 3.3: The regression coefficients, p values and Pearson correlation coefficients for R2t* vs. Thickness and R2t* (s^{-1}) vs. OEF_{rel}. Data represent averages from 20 healthy subjects across 26 selected FreeSurfer ROIs displayed in Figure 3.3.

The regional characteristic values of R2t* and thickness correspond to a_{ROI} from Equation (3.3). Since OEF_{rel} remains constant with age in the cortical regions, the characteristic values of OEF_{rel} are just the mean values across the subjects in the corresponding regions. R2t* correlates negatively with the cortical thickness across 26 cortical ROIs ($p < 0.05$ and $r = 0.71$, Figure 3.3a). This correlation indicates that the thinner cortex has a relatively higher R2t*. Furthermore, R2t* positively correlates with OEF_{rel} across 26 cortical ROIs ($p < 0.05$ and $r = 0.8$, Figure 3.3b). The regions extracting more oxygen also have higher R2t*. Implications of all these correlations will be discussed in detail in the Discussion section.

3.3.4 Age-related Changes of R2* in Subcortical Regions

Table 3.4			
ROI	R2* (s^{-1})		
name	slope	intercept	p value
caudate	0.094	21.4	0.0003
putamen	0.209	24.0	0.0003
pallidum	0.178	34.8	0.0004
thalamus	0.013	21.0	0.1635
hippocampus	0.024	16.9	0.0816
amygdala	0.035	15.4	0.0341

Table 3.4: The regression coefficients and p values of R2* vs. age in 6 subcortical ROIs. Data represent results from 20 healthy subjects displayed in Figure 3.4.

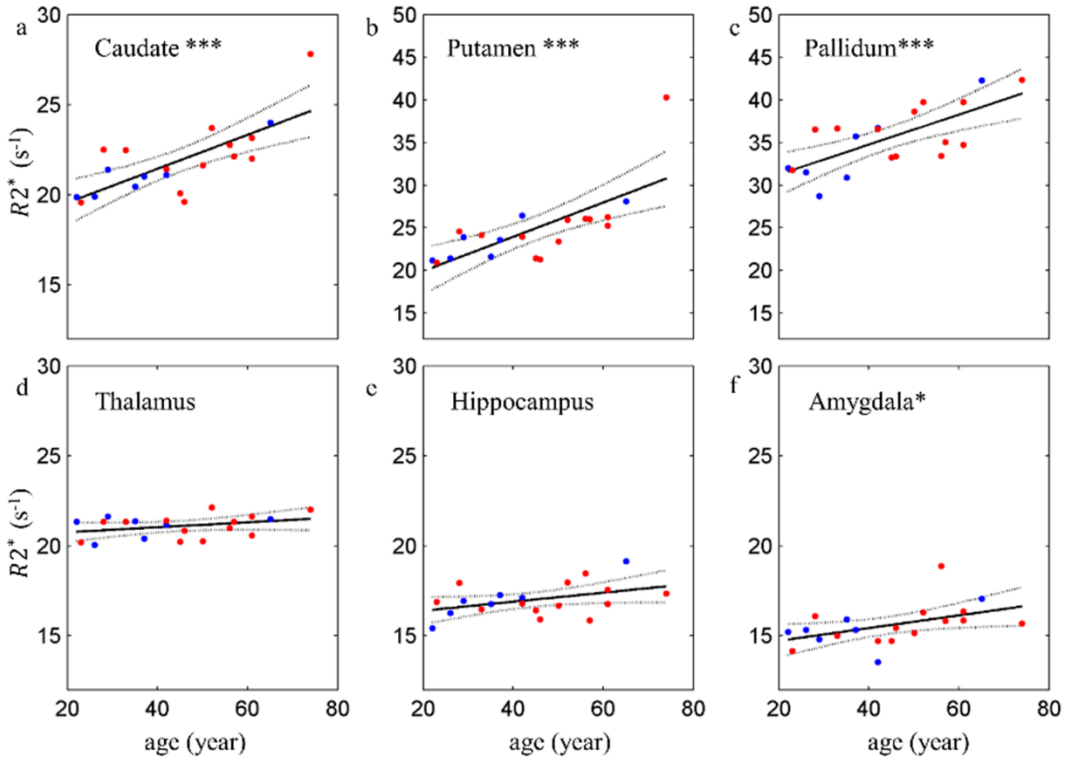

Figure 3.4 The scatter plots and linear regressions of R2* versus age in subcortical ROIs. Each plot represents the data from a single subcortical region and each point in the plot represents the median value in the region from a single subject. Male subjects are represented by blue points and female subjects by red points. The solid lines are the regression curves and the dashed lines are the 95% confidence intervals. All the coefficients from the linear regressions are listed in Table 4. $p < 0.001$ ***, $p < 0.01$ **, $p < 0.05$ *.

R2* significantly increases with age in basal ganglia (caudate, putamen and pallidum), and amygdala. Thalamus and hippocampus show less significant age-related changes. Notice that R2* in the basal ganglia is substantially larger than R2* in the cortex. This is because basal ganglia is rich of iron deposition, which is paramagnetic and cause R2* to increase significantly.

3.2.5 Error Analysis

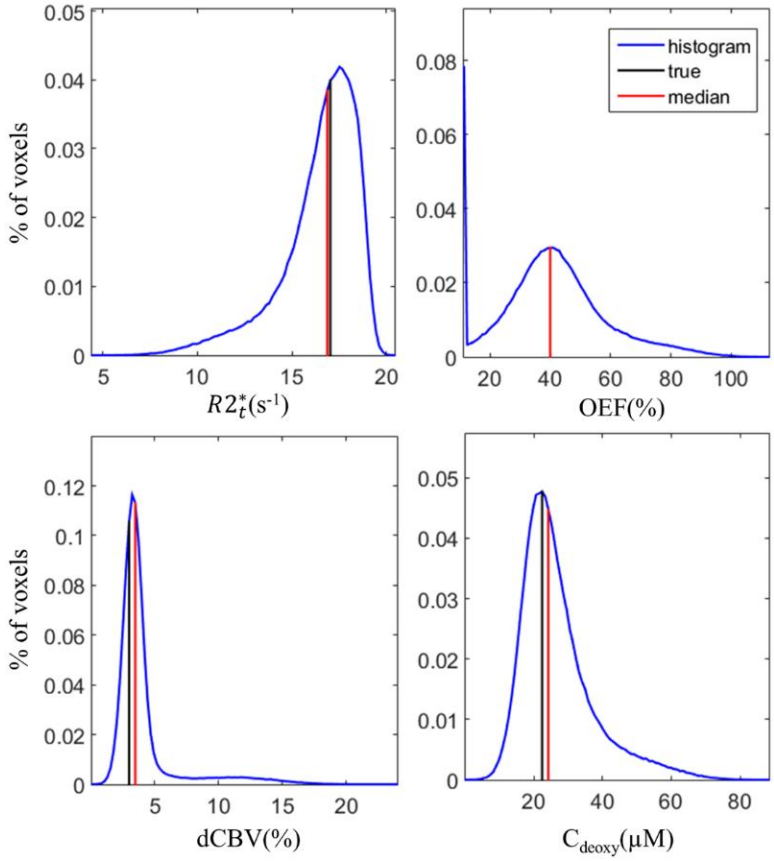

Figure 3.5 The histograms of the simulated data for R2t*, OEF, dCBV and C_{deoxy} are shown with true values (black) and median values (red). The black and red lines overlap in the histogram of OEF. Note that the peak in OEF histogram at the lower boundary is due to the restriction set in the fitting routine (OEF > 10%).

Table 3.5					
	A_0	R2t* (s^{-1})	OEF (%)	dCBV (%)	C_{deoxy} (μM)
true values	100.00	17.00	40.00	3.00	22.44
median	99.94	16.91	40.01	3.43	24.63
mean	99.85	16.44	40.80	4.12	27.04
standard deviation	0.75	2.06	17.32	2.60	10.73

Table 3.5: The true values, medians, means and standard deviations of all the parameters in the simulations are listed here. The medians more accurately represent true values than the means for all the parameters.

The results are listed in Table 3.5. The histograms of the output parameters, and the corresponding true and median values are shown in Figure 3.5. The results show that the median values of R2t*, OEF, dCBV and C_{deoxy} better represent the true values than the means because the histograms are skewed and the median is less biased by the outliers.

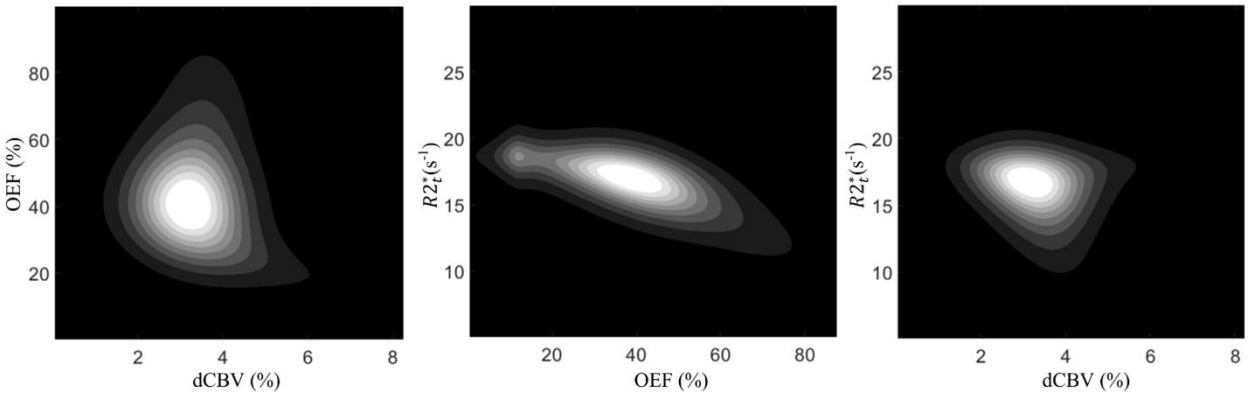

Figure 3.6 The contour covariance maps of the simulated data. The results show the peak values of R2t* around 17, OEF around 40% and dCBV around 3%, well estimating the true values. The covariance between OEF and dCBV is consistent with the actual covariance map between the OEF and dCBV presented in Fig. 6 in the previous publication by Ulrich and Yablonskiy (5).

The 2D contour covariance maps of the relationships between R2t*, OEF and dCBV are shown in Figure 3.6. It demonstrates the peak value of R2t* around 17, OEF around 40% and dCBV around 3%, well estimating the true values. The negative correlation between R2t* and OEF ($r = -0.88$, $p < 0.001$) strengthens that the observed positive correlation between R2t* and OEF_{rel} in our experimental data (Figure 3.3) reflects the physiological relationship instead of errors.

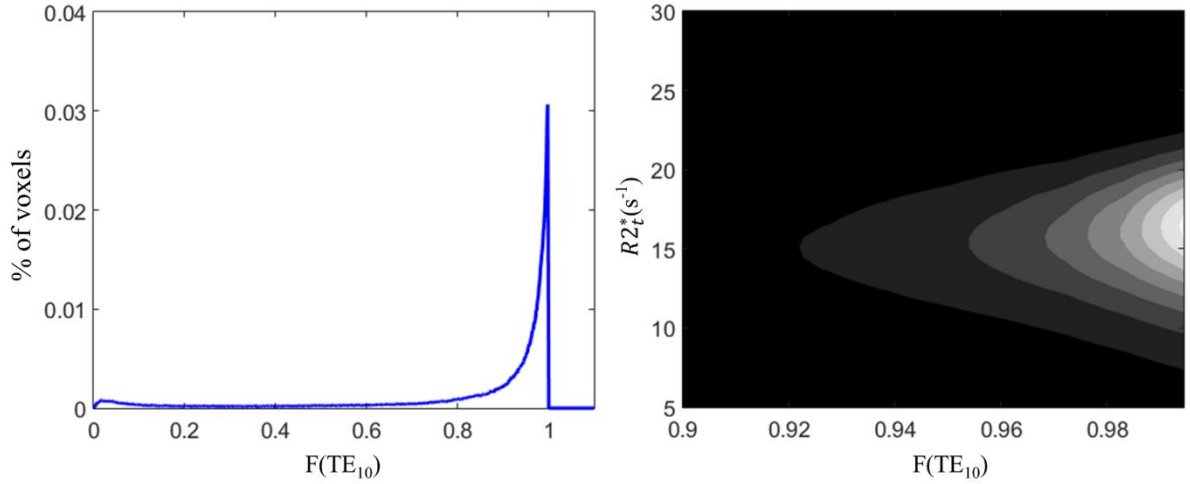

Figure 3.7 Typical example of the distribution of $F(TE_{10})$ and the joint covariance contour of R2t* and $F(TE_{10})$ are shown for a single subject. The range of $F(TE_{10})$ is from 0 to 1 and most of values are between 0.9 to 1. The number of voxels with $F(TE_{10})$ lower than 0.8 is quite small and they are not visible on the contour map. No covariance is found between R2t* and $F(TE_{10})$ suggesting no bias in R2t* estimate due to the field inhomogeneities.

The detailed analysis of the correction for field inhomogeneity artifacts was provided in Yablonskiy lab's previous paper where voxel spread function method (3) was introduced. Here we further demonstrate that VSF procedure does not create bias in parameters estimates in our data. The signal decay due to the macroscopic field inhomogeneities is characterized by the *F* function at the last echo, $F(TE_{10})$, where the strongest signal decay is observed. Example of the distribution of *F* function at the last echo, $F(TE_{10})$, and the contour map of the joint covariance between R2t* and $F(TE_{10})$, for the whole gray matter from an individual subject is shown in Figure 3.7. No correlation is found between R2t* and $F(TE_{10})$. The peak value of $F(TE_{10})$ is around 0.99 and most of values are located between 0.9 and 1 due to a good shimming procedure and rather small voxel size. The number of voxels with values lower than 0.8 is so small that they are not visible on the contour map. These voxels with lower $F(TE_{10})$ are mostly affected by

the magnetic inhomogeneity due to the air/water interface around the sinuses and represent a very small fraction of the brain.

One additional bias in the parameter estimates may be related to the estimation of OEF. Because the BOLD model is developed under the assumption that the orientations of blood vessels are statistically random in each voxel, the actual variations of the blood vessel orientations may cause deviations in estimating OEF on a voxel by voxel basis. For example, if the blood vessels in some voxels have the predominant orientation parallel to the static magnetic field B_0, the BOLD effect is so minimal that the fitting routine will substantially underestimate OEF; conversely, OEF will be underestimated for the voxels with the predominant orientations of blood vessels perpendicular to B_0. However, as demonstrated in (8), the estimates of R2t* and dCBV are not affected by this limitation. Besides, the use of median values for representing our results for very large regions, also minimizes these biases.

In conclusion, although substantial deviations from the true values of all parameters can be found in individual voxels and there are several restrictions on this model, the medians values of the parameters are very close to the true values. All in all, the simulations support that the methodology used in this study can generate the valid regional medians of R2t* and hemodynamic parameters for large cortical regions. In my dissertation, the results in cortical regions usually contain thousands of voxels.

3.4 Discussion

The result section shows the relationship between GEPCI derived parameters and age across cortical ROIs, which achieve the first goal of this study. The second goal is to interpret these

results and find out the biological meaning of GEPCI derived parameters, especially for R2* and R2t*. The key questions are: why R2t* increases with age in the cortex and what features of the brain cellular structure cause this increase and variability between different brain structures? Main contributions to R2t* signal decay in different brain structures come from the water molecules interactions with cell structural proteins, lipids and iron (80-82). In the subcortical GM, i.e., the caudate, putamen and pallidum, a significant increase in R2* with age that we observed (Fig. 4), is consistent with previous studies (82-87) and is usually attributed to the known iron deposition in those regions with the increasing age. However, iron is unlikely a contributor to the age-related increase of the cortical R2t* because, according to Hallgren and Sourander (88), the iron content in the cortex remains nearly constant after the age of 30. The major contributions to the increased cortical R2t* and its variability are likely to be attributed to the water molecule interactions with other cellular structural components such as lipids and proteins.

Another source of the variation in R2* potentially could be an anisotropic effect reported by Rudko et al (89). However, even at 9.4T field strength, R2* showed only 0.94 ± 0.32 s^{-1} variation in GM of mice, which is a much smaller effect than the variation across different brain regions that we found in a human brain at 3T.

The hypothesis that the changes of MR signal relaxation properties are related to the changes in the concentration of lipids and proteins has been useful in studying Central Nervous System (CNS) diseases, such as Multiple Sclerosis (e.g., (69, 90)) where cellular damage is mostly attributed to the loss of myelin. However, this hypothesis might not be adequate to describe normal aging effects of a healthy tissue where MR signal relaxation properties are related not only to the concentration of the cellular structural components but also to their cellular structural

arrangements (91). For example, lipids distributed as multiple small droplets would have much bigger water-accessible surface, hence cause substantially stronger relaxation effects than a single large lipid droplet with the same total amount of lipids.

Herein by comparing our results with the literature data about normal aging (reviewed in Chapter 2) we provide support for a hypothesis that in a healthy adult brain the tissue-specific R2t* can serve as a biomarker of the cortical "cellular packing density", which is mostly proportional to the number of neurons and glial cells in the unit tissue volume. We also use this hypothesis to explain the relationships between R2t* and the functional data, such as OEF and aerobic glycolysis.

3.4.1 Cortical Cellular Packing Density is related to R2t*

Our hypothesis is supported by the available literature data on the cellular changes in the aging brain. As reviewed in Chapter 2, it was a common impression that the neuron loss (20, 21) is an inevitable process of aging that leads to the cortical thinning and cognitive dysfunction. However, many studies have reported that the number of neurons in the human cortex remains the same over adult life (19, 22-26, 35, 92) and that normal aging is accompanied by changes in the dendritic structures, spine density and synapse density. Even the total number of glial cells in the cortex remains relatively constant over normal adult life (25, 27). The unchanged number of cells and the decreasing cortical volume imply the increasing cell density with age in the cortex, which is also supported by previous studies (23, 26, 31).

This increasing age-related cortical cellular packing density in the cortex is consistent with our interpretation of age-related increased R2t* reported herein as a biomarker of cellular packing density. In this context, the product of R2t* and cortical thickness, SR2t*, represents the cellular packing content underneath a unit surface (e.g., 1 square millimeter surface) of the cortex. Our

finding that this product remains constant with age for all cortical regions (Figure 3.1g, Table 3.1), is in agreement with the preservation of cortical cellular content in healthy adults over age.

If both the number of neurons and the relative fraction of glial cells to neurons stay the same over age, the density of both neurons and glial cells would go up proportionally. Since axons and dendrites contain considerably larger concentration of macromolecules (e.g., lipids and proteins), their contribution to the R2t* relaxation is expected to be prevailing compared to glial cells even though concentration of glia cells in the cortex is higher. Hence, we hypothesize that the increase of R2t* is mainly due to the increased neuronal density.

3.4.2 Neuronal Density of Non-human Primates is related to R2t*

Our data is also compared with the neuronal density of non-human primates measured by Collins et al. (93). Collins et al. reported the highest neuronal density in primary visual cortex, the second highest in association visual areas and relatively higher density in primary somatosensory areas (S1) among all of the examined primates. Lowest neuronal densities were found in prefrontal cortex, premotor cortex or cortex ventral to S1 and motor cortex (M1) in different primates. Those distributions of neuronal density are in a good association with the distributions of R2t*. Indeed, the highest R2t* were found in the visual cortex (cuneus, lateral occipital and lingual) and the lowest were found in the frontal areas (Figure 3.2 and Table 3.1). Relatively higher R2t* were also shown in S1 and M1 (paracentral, precentral and postcentral) and R2t* values in these two regions were similar. Relatively lower R2t* were found in regions close to S1 and M1. All in all, these data further support our hypothesis that R2t* is related to neuronal or cellular packing density.

Elston et al. (94) found that cells in the prefrontal cortex of humans are more branched and more spinous than those in the temporal and occipital lobes. Comparing these results with the

measurements of neuronal density by Collins et al. (93) we can conclude that regions with relatively lower neuronal density have more complex dendritic arbors, larger somas and dendritic field sizes and more spines than regions with higher neuronal density. This is in agreement with the line of consideration by Glasser and Van Essen (95) who utilized T1- and T2-weighted MRI to evaluate a distribution of the myelin content in the cortex. Hence, comparing the R2t* maps with these literature data (93, 94), we can further suggest that the areas with lower R2t* represent regions with complex dendritic arbors, larger somas and dendritic field sizes and more spines than regions with higher R2t*.

3.4.3 Brain Tissue Hemodynamic Properties

Besides R2t*, the relative OEF, dCBV and C_{deoxy} are also derived from GEPCI data and they are in agreement with previous literature results. The distribution of the relative OEF in Figure 3.1 shows the uniformity across frontal area and precuneus but higher values in the visual cortex (cuneus and lingual) which is consistent with the findings of default mode network (96). The relative OEF shows no significant change with age (Figure 3.2c), which is consistent with previous studies. Leenders *et al*. reported that oxygen extraction fraction (OER) didn't change or showed a slight increase with age in the selected regions (97). Pantano *et al*. showed that OEF had no statistically significant changes with age, although a small upward trend was present (98). Yamaguchi *et al*. also demonstrated that OEF didn't show any correlation with age (99). GEPCI dCBV shows no significant change with age which is consistent with previous findings of no significant changes in the cerebral blood volume (which is a measure of both, dCBV and arterial blood volume) with age (97, 99).

The R2t* map outlines practically the same pattern as the map of aerobic glycolysis (100) with areas of low R2t* corresponding to areas of high aerobic glycolysis and areas of high R2t*

corresponding to areas of low aerobic glycolysis. This fits well with our biophysical hypothesis of R2t* reflecting cellular packing density. Indeed, the areas of complex dendritic and synaptic structures characterized by lower R2t* are likely to require high aerobic glycolysis needed to support high synaptic activities (101). Moreover, since the correlation in brain regions between aerobic glycolysis and CBF is stronger than that between aerobic glycolysis and $CMRO_2$ (101), areas of high aerobic glycolytic activity may show relatively lower OEF. Hence, it explains the strong correlation between R2* and OEF ($p < 0.001$, $r = 0.71$ in Figure 3.2b). It is also important to note that the regions with lower R2t* are mostly located within the default mode network (96).

Although OEF and R2t* are derived from the same data and model, their correlation is robust. Computer Monte-Carlo simulations (15) demonstrated that bias in the estimation of R2t* due to using static dephasing regime model (11) does not exceed 0.3 s^{-1} and biases in OEF and dCBV are smaller than 10%. Furthermore, Figure 3.6 shows that the correlation between R2t* and OEF_{rel} is negative due to the noise of the data and fitting routine. Hence, the observed positive correlation is due to the biological environment in the human brain. Besides, the results are consistent with the above listed literature data.

3.4 Summary

Distinguishing the cognitive changes of normal aging from the initial stages of neurodegenerative disorders, such as Alzheimer's disease, can be difficult. Hence, establishing baseline MRI biomarkers for normal aging is significant and valuable. In this study, we used an advanced GEPCI approach (3-5) allowing the quantitation of various tissue specific structural and functional metrics.

Comparison between GEPCI data and the available literature information suggests that the age-related increase in the cortical R2t* mostly reflect the age-related increase in the cellular packing density. GEPCI data also show that tissue hemodynamic parameters, i. e. relative OEF, dCBV and C_{deoxy} have no linear correlations with age and remain practically constant in most cortical regions. We found important correlations characterizing relationships between brain structural and hemodynamic properties in different brain regions. Specifically, thicker cortical regions have lower R2t*, reflecting less cellular packing density, and these regions extract less oxygen from the blood.

All our findings can be understood if we put forward the following hypotheses:

1. Regions in a brain characterized by a higher R2t* contain higher concentration of neurons with less developed cellular processes and are characterized by lower glycolytic activity. Accordingly, they require less blood flow to maintain their structure. These areas have higher OEF.

2. Regions in a brain characterized by a lower R2t* represent regions with lower concentration of neurons but more developed cellular processes (dendrites, spines, etc.). They display higher glycolytic activity, hence require higher blood flow to maintain and develop new structural elements responsible for "information storage". These areas have lower OEF.

Chapter 4: In vivo Detection of Microstructural Correlates of Brain Pathology in Preclinical and Early Alzheimer's Disease with MRI

4.1 Introduction

Based on the biological interpretations of GEPCI metrics in Chapter 3, we now apply GEPCI metrics to Alzheimer's disease (AD). As reviewed in Chapter 2, Alzheimer's disease (AD) is a neurodegenerative disorder that is characterized by intraneuronal aggregates of tau called neurofibrillary tangles and extracellular aggregates of amyloid-beta (Aβ) protein called plaques. Clinically, AD is characterized by memory deficits and progressive cognitive impairment, leading to dementia. The preclinical stage of AD provides a large window for therapeutic intervention (102). Hence, one of the important directions is developing widely accessible neuroimaging techniques that can detect AD brain pathology in the preclinical stages (103, 104).

One of the prevailing hypotheses of AD is the amyloid cascade hypothesis (36, 39, 41, 42) that suggests that abnormal accumulation of (Aβ) in the neocortex is one of the earliest pathological markers of AD. Paradoxically, it is also known that the medial temporal lobe (MTL), a region that mediates short-term memory, is affected early in the disease but is not the most affected region by Aβ deposition compared with neocortical regions (e.g., prefrontal cortex and precuneus (47-49)). At the same time, histological studies show that the MTL is particularly vulnerable to neurofibrillary pathology in the early stages of aging and AD (65, 66, 105-108). The reduction of volume and the loss of cells in the entorhinal cortex and hippocampus have been extensively reported in participants with mild cognitive impairment (MCI) and AD (57-61). Importantly,

neuropathology studies have established that symptomatic AD begins only when cell loss occurs in the hippocampal area (59).

MRI is a potentially powerful tool to identify changes in the Alzheimer brain. Most MRI studies so far have focused on AD-related volumetric measurements of brain atrophy (109). A few studies attempted to identify plaques via MRI in postmortem specimens or mice models (110-115), though the latter methods require long imaging time and have not been translated to human studies.

The goal of this study was to establish the relationship between GEPCI metrics and AD-related tissue damage at preclinical and very early symptomatic stages of AD. To this end, participants were enrolled from the Washington University Knight Alzheimer's Disease Research Center (Knight ADRC) with well-characterized clinical status ranging from cognitively normal to very mild and mild AD, and with a battery of psychometric, CSF and neuroimaging data. We demonstrated a significant correlation between GEPCI metrics of brain tissue cellular damage in the hippocampus and cognitive performance. Importantly, this correlation is stronger than the correlation between cognitive performance and hippocampal atrophy, thus suggesting that the integrity of the remaining tissue is a more important parameter for brain functioning than the loss of tissue volume alone. We also uncovered a remarkable correlation between GEPCI metrics and beta-amyloid load measured by positron emission tomography (PET) (the current *in vivo* gold standard), thus supporting GEPCI as a potential surrogate marker for Aβ imaging in preclinical and early Alzheimer disease.

The results demonstrate that GEPCI is sensitive to early AD-related pathological changes in brain tissue. Since the GEPCI approach is based on MRI that is widely available worldwide, is non-invasive, and does not require radiation exposure, it can open opportunities to obtain new

information on the pathogenesis of AD. The new method can also open the door for screening cohorts for clinical drug trials (stratification) that are enrolling individuals with preclinical or early symptomatic AD.

4.2 Methods

4.2.1 Participants

This study was approved by the Institutional Review Board of Washington University School of Medicine (WUSM). 34 participants were selected from the studies of aging and dementia at the Knight Alzheimer's Disease Research Center (ADRC) at WUSM. All participants provided informed consent. All participants in this study underwent a collection of cognitive performance tests (116), including Free and Cued Selective Reminding Test (Srtfree), Animal Naming (ANIMALS), and Trail making Test Part A (Tma) . Cognitive status was operationalized with the Clinical Dementia Rating (CDR) (67), as determined by Knight ADRC clinicians according to standard protocols; diagnoses were in accordance with standard criteria (38). The participants were assessed to be cognitively normal (CDR = 0) or to have mild (CDR = 0.5 or 1) AD dementia. 19 participants underwent PiB PET imaging to estimate amyloid deposition in the gray matter and white matter of their brains. The measurements of CSF biomarker $A\beta_{42}$ (INNOTEST, Fujirebio, Gent, Belgium) were available for 31 participants. For participants that underwent PiB PET imaging, amyloid positivity was defined by a cutoff of mean cortical binding potential (MCBP)=0.18 (117) which corresponds to a mean cortical standardized uptake value ratio (MC-SUVR) of 1.3 referenced to cerebellar grey matter. MC-SUVR for Aβ imaging is calculated as the averaged SUVR of regions within the prefrontal cortex, gyrus rectus, lateral temporal, and precuneus regions. For participants that did not have PET Aβ measurements, Aβ positivity was

determined by the status of their CSF biomarker $A\beta_{42}$ (103). According to the Aβ status, cognitively normal participants (CDR = 0) were further divided into normal (CDR = 0; Aβ negative) and preclinical (CDR = 0; Aβ positive) groups. Notice that one participant with CDR = 0.5 and one with CDR = 1 had negative Aβ status. Demographic information for all groups is presented in Table 4.1.

Table 4.1			
	Normal	Preclinical AD	Mild AD
	CDR=0 Aβ negative	CDR=0 Aβ positive	CDR=0.5 or 1
N	13	10	11 (7/4)
Age	69.6±8.7	72.3±8.4	76.0±8.4
Female/Male	7/6	4/6	3/8

Table 4.1 Distribution of participants between groups and their demographic information. Note that nine participants in Mild AD group were Aβ positive and two were Aβ negative.

4.2.2 MRI Data Acquisition

All participants were scanned in a 3T PET-MR scanner (Siemens, Erlangen, Germany). A 3D multi gradient echo sequence was used to obtain the data. Sequence parameters were: resolution $1\times1\times2$ mm^3 (read, phase, slab), FOV 256 mm×192 mm, repetition time TR = 50ms, flip angle 30°, 10 gradient echoes with first gradient echo time TE_1 = 4 ms, echo spacing ΔTE = 4ms. Additional phase stabilization echo (the navigator data) was collected for each line in k-space to correct for image artifacts due to the physiological fluctuations (4). The total acquisition time of GEPCI was 11 mins 30s. Macroscopic field inhomogeneity effects (background gradients) were accounted for by using the voxel spread function (VSF) approach (3). Standard clinical Magnetization-Prepared Rapid Gradient Echo (MPRAGE) (75) images with TR/TI/TE =

2200/1100/3.37 ms and the resolution 1×1×1 mm^3 were also collected for segmentation purposes. The total acquisition time of MPRAGE is 6 mins.

4.2.3 Data Analysis and GEPCI Images Generation

This part was the same as Chapter 3, which was described in details in Chapter 1. Herein, I briefly introduce the model and fitting parameters:

$$\begin{aligned} S(TE) &= A_0 \cdot \exp\left(-R2^* \cdot (TE + TE_1) + i \cdot 2\pi \cdot \Delta f \cdot (TE - TE_1)\right) \cdot F(TE) \\ S(TE) &= A_0 \cdot \exp\left[-R2t^* \cdot (TE - TE_1) + i \cdot 2\pi \cdot \Delta f \cdot (TE - TE_1)\right] \cdot F_{BOLD}(TE) \cdot F(TE) \end{aligned} \quad (4.1)$$

where TE is the gradient echo time, R2*=1/T2* is the global transverse relaxation rate constant, R2t*=1/T2t* is the tissue transverse relaxation rate constant in the absence of BOLD effect, Δf is the frequency shift (dependent on tissue structure and also macroscopic magnetic field created mostly by tissue/air interfaces), function $F_{BOLD}(TE)$ describes GRE signal decay due to the presence of blood vessel network with deoxygenated blood, and function F(TE) describes the effects of macroscopic magnetic field inhomogeneities.

By fitting the equation to the real and imaginary parts of the complex signal using nonlinear regression algorithm, six parameters are computed: A_0 (T1-weighted), R2*, R2t*, Δf, ζ and $\delta\omega$ for each voxel in the brain. In this study, we focus on total R2* and tissue specific R2t* measurements for quantifying tissue microstructural properties and GEPCI T1W images (the square root of parameter A_0) for brain structure delineation and segmentation.

Notice that $F_{BOLD}(TE)$ in Equation 4.1 was originally designed to describe the signal decay due to the presence of different types of magnetic susceptibility inclusions, such as blood vessel network (BOLD effect), trabecular bone and iron oxide nanoparticles, etc. (11). It has different formulas for different inclusions and the one we used in this study is modeled for the blood

vessel network. But in the context of AD, $F_{BOLD}(TE)$ may also include the mesoscopic inhomogeneity effects created by amyloid plaques that are known to create *R2** signal decay (115). As a result, R2* is more related to the amyloid deposition while R2t* is more related to the tissue structure.

4.2.4 Image Segmentation

The segmentation part is also the same as Chapter 3. FreeSurfer software (Laboratory for Computational Neuroimaging, Martinos Center for Biomedical Imaging) (76) was used to generate brain segmentations, cortical thicknesse and volume based on MPRAGE images. Then, MPRAGE images are registered to GEPCI-T1-weighted (T1W) images using FMRIB's Linear Image Registration Tool (77, 78) in FSL and the transformation matrices of the registration are generated. Finally, these matrices were applied to the brain segmentations from FreeSurfer and transformed to the space of GEPCI-T1W images. One of the important advantages of GEPCI is that all GEPCI images are generated from a single MRI scan and are naturally co-registered. Hence, segmentations of GEPCI T1W images were naturally co-registered with all other GEPCI maps.

A CSF mask from FSL is further applied removing voxels in CSF on FreeSurfer segmentations. To maximize accuracy of measurements, statistical results instead of voxel-wise analysis are reported: for each FreeSurfer region containing thousands of voxels, a single parameter – mean value of GEPCI parameter, is generated.

4.3 Results and Discussions

In the context of AD, we hypothesize that the increased beta-amyloid deposition should lead to an increase in GEPCI R2* that is sensitive to mesoscopic field inhomogeneities (8, 11). The

mesoscopic field inhomogeneities may be present around amyloid deposits and can be enhanced due to the presence of iron in amyloid plaques (111). On the other hand, cellular loss characteristic of AD can lead to decreased GEPCI metrics, especially R2t* that is sensitive to cellular structure (12). The interplay between these two opposing processes can define important features of the GEPCI signal in AD.

4.3.1 Correlation between R2* and PiB-PET Aβ Measurement

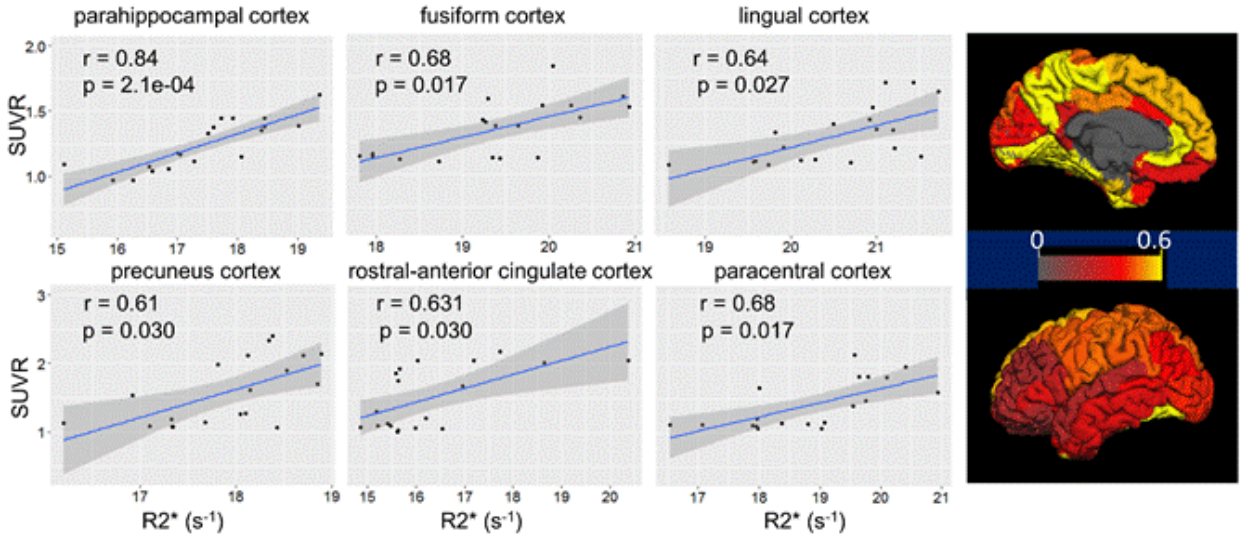

Figure 4.1 Correlation between PiB PET Aβ SUVR (dimensionless) and R2* (s^{-1}) relaxation rate constant obtained in 19 participants. Plots show examples of correlation in several brain regions. Each point represents a single participant. Shaded areas represent 95% confidence intervals of the linear fits (solid lines). Pearson correlation coefficients (r) and p values (corrected for multiple comparison using false discovery rate over all cortical regions) are shown in the left upper corners. The surface maps on the right represent r values in all cortical areas. The image segmentation is based on the FreeSurfer software (76). The data show significant correlations not only in the areas of high Aβ accumulation (e.g., precuneus) but also in the areas of MTL, such as the parahippocampal cortex and the fusiform cortex. Particularly, the strongest and most significant correlation exists in the parahippocampal cortex.

The correlation analysis between R2* and PiB PET Aβ measurements (using standardized uptake value ratio [SUVR]) revealed positive correlations in most cortical brain regions. The data

showed significant correlations not only in the areas of high Aβ accumulation (e.g., precuneus) but also in the areas of MTL, such as the parahippocampal cortex and the fusiform cortex. But not all correlations were statistically significant after correction for multiple comparison using false discovery rate (FDR) (118), most likely due to the small sample size (PiB PET data were available only for 19 participants). Examples of the correlations with significant p values are shown in Figure 4.1.

The strongest correlation between R2* and Aβ SUVR that we found in the parahippocampal cortex shows the high sensitivity of GEPCI R2* to Aβ accumulation in this area. Interestingly, although the range of SUVR in parahippocampal cortex is smaller than in precuneus, the correlation in parahippocampal cortex is much stronger than that in precuneus. It indicates that even though MTL is not the area of the highest burden of Aβ in the AD brain, it represents a very important area of pathological changes in early AD particularly as it relates to the formation of Aβ plaques in the cerebral cortex, where the changes can be detected by GEPCI R2*. This feature likely can be attributed to distinct cellular properties of the gray matter in the MTL that play important roles in functionally connecting the neocortex and hippocampus (119). Structurally, the parahippocampal gyrus is a transitional zone, where the entorhinal cortex (referred as perialocortex) contains the lamina dissecans while the perirhinal and parahippocampal cortexes (referred as proisocortex) have their cellular structure different from the major three-layered and six-layered cortex areas (120). As different cellular components and arrangements contribute to R2*, it is possible that the strong correlations between R2* and Aβ SUVR in the parahippocampal cortex is due to its unique laminar organizations. Since the medial portion of the fusiform gyrus is also considered to be part of the parahippocampal cortex, it is

reasonable to observe the significant correlation between R2* and Aβ SUVR in the fusiform as well.

How can we interpret the correlation? As we discussed in Methods, $F_{BOLD}(TE)$ may also include the mesoscopic inhomogeneity effects created by amyloid plaques that are known to create *R2** signal decay (115). Since no correlation exists between amyloid accumulation and BOLD effect (100), the correlation between amyloid accumulation and *R2** is mostly related to magnetic susceptibility effects created by amyloid plaques. A hypothesized iron deposition in amyloid plaques (111, 121) could lead to additional sensitivity of GEPCI *R2** to Aβ accumulation.

The presence of neurofibrillary tangles (NFTs) and neuronal loss in the parahippocampal gyrus previously reported by Thangavel *et al* (65) can also affect R2*. However, their participants were assessed at death after nearly a decade of dementia, while the cohort in this study represents mostly normal, pre-symptomatic, very mild (CDR = 0.5) or mild (CDR=1) AD. In addition, as tissue damage in the parahippocampal gyrus was smaller than that in the hippocampus (66), in our cohort the loss of neurons in the parahippocampal gyrus may not be severe enough to affect R2* measurements.

Even though the significance of the correlations between R2* and Aβ SUVR vary for different brain regions, R2* in the parahippocampal cortex can still be used for evaluation of Aβ burden in all regions. Indeed, the data show very strong correlations between Aβ SUVR in most cortical regions and R2* values in the parahippocampal cortex. These correlations can be described as follows:

$$SUVR_{ROI} = a_{ROI} + k_{ROI} \cdot (R2^*_{PH} - \bar{R2}^*_{PH}) \qquad (4.2)$$

and can be used for evaluation of Aβ SUVR for a given participant in any cortical region. In Equation (4.2), $R2^*_{PH}$ is $R2^*$ in the parahippocampal cortex for a given participant, and $\overline{R2^*_{PH}}$ = 16.55 sec^{-1}, is the mean value of R2* in the parahippocampal cortex of the normal control group (9 participants with negative PiB Aβ and CDR = 0). The coefficients a_{ROI} and k_{ROI} in Equation (4.2), specific for each cortical ROI, are provided in Table 4.2 along with the results of the correlations. $\overline{R2^*_{PH}}$ is introduced in Equation (4.2) to make the coefficients a_{ROI} of the regression more meaningful – they represent region-specific averaged SUVR for healthy control group. The slopes of the regression (parameter k_{ROI}) are also shown in Figure 4.2, upper row. The spatial pattern in Figure 4.2 is similar to previously established correlation pattern between regional and mean values of PiB SUVR (122). Hence, the data demonstrate that R2* in the MTL (especially the parahippocampal cortex) not only correlate with PiB PET SUVR in this area but also strongly correlate with PiB PET SUVR throughout the entire cortex.

Table 4.2				
Cortical area	Intercept (*a*)	Slope (*k*, sec)	p value	r
bankssts	1.35	0.24	2.47E-04	0.75
caudal-anteriorcingulate	1.23	0.27	2.45E-04	0.75
caudal-middlefrontal	1.16	0.24	1.76E-04	0.76
cuneus	1.22	0.12	2.79E-02	0.50
entorhinal	1.10	0.08	1.33E-04	0.77
frontalpole	1.07	0.30	5.31E-04	0.72
fusiform	1.21	0.15	2.02E-04	0.75
inferiorparietal	1.21	0.23	4.08E-04	0.73
inferiortemporal	1.15	0.20	4.63E-04	0.72
insula	1.23	0.18	2.90E-04	0.74
isthmuscingulate	1.34	0.25	5.46E-04	0.72
lateraloccipital	1.15	0.12	1.22E-03	0.68
lateralorbitofrontal	1.26	0.25	4.45E-04	0.72
lingual	1.19	0.12	6.46E-03	0.60
medialorbitofrontal	1.23	0.32	2.98E-04	0.74
middletemporal	1.13	0.21	1.73E-04	0.76
paracentral	1.21	0.23	1.00E-03	0.69
parahippocampal	1.11	0.15	6.09E-06	0.84
parsopercularis	1.19	0.23	4.66E-04	0.72
parsorbitalis	1.13	0.26	4.97E-04	0.72
parstriangularis	1.20	0.24	3.90E-04	0.73
pericalcarine	1.27	0.14	2.56E-02	0.51
postcentral	1.07	0.15	2.02E-03	0.66
posteriorcingulate	1.29	0.32	4.58E-04	0.72
precentral	1.14	0.14	9.57E-04	0.70
precuneus	1.30	0.32	5.93E-04	0.71
rostralanteriorcingulate	1.23	0.31	2.28E-04	0.75
rostralmiddlefrontal	1.16	0.30	4.34E-04	0.73
superiorfrontal	1.14	0.28	3.25E-04	0.74
superiorparietal	1.15	0.21	6.31E-04	0.71
superiortemporal	1.15	0.18	2.45E-04	0.75
supramarginal	1.16	0.21	6.68E-04	0.71
temporalpole	1.11	0.10	9.94E-04	0.69
transversetemporal	1.21	0.18	4.48E-04	0.72

Table 4.2. The results of linear regression analysis of the relationship between regional amyloid SUVR in different cortical regions and the parahippocampal R2*. Cortical regions are selected based on the FreeSurfer segmentation (76). The data show coefficients of linear regression in Equation (4.2) and the correlation coefficients (*r*). The mean value of R2* in the parahippocampal region for the control group in Equation 4.2 is 16.55 sec^{-1}.

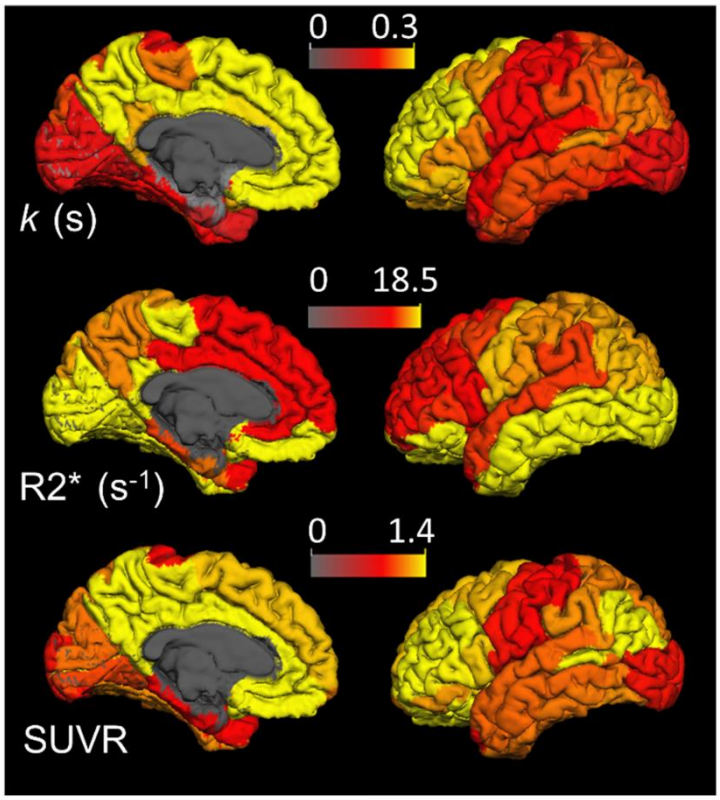

Figure 4.2 Upper row represents the surface maps of the slopes (units of sec) of linear regression (coefficient k_{ROI} in Equation (4.2)) between regional PET-measured Aβ SUVR and parahippocampal R2* across 19 participants. All regional slopes are positive. The coefficients of the linear regressions are listed in Table 4.2. The second and the last rows represent the averaged cortical mean values of R2* and Aβ SUVR across the same 19 participants. White matter, deep gray matter and ventricles were excluded. The image segmentation is based on the FreeSurfer software (76).

While the data show rather significant positive correlations between R2* and amyloid burden across the participants in different brain regions (Figure 4.1), there also exists an *inverse association* across the brain regions between averaged R2* and amyloid distributions. Figure 4.2 shows regional R2* and Aβ SUVR averaged across 19 participants mapped onto the brain surface. Lower R2* are found in the frontal cortex, posterior cingulate, precuneus, parahippocampal cortex, entorhinal cortex and superior temporal cortex. Higher R2* are found in the occipital cortex, paracentral cortex, fusiform, middle and inferior temporal cortex. This R2*

distribution is consistent with the previous studies (12). In contrast to the R2*, the PiB retention was prominently higher in the frontal cortex, posterior cingulate, precuneus and inferior parietal cortex, which is also consistent with the previous reports (44, 47). Generally speaking, PiB Aβ binding tends to increase in the regions with lower R2*, which may indicate that the regions with lower R2* are more vulnerable to the amyloid accumulation. This relationship is more obvious in the frontal cortex, posterior cingulate, precuneus, inferior parietal cortex characterized with higher SUVR but lower R2*, and occipital cortex with lower SUVR but higher R2*. Interestingly, the former regions mostly overlap the default mode network (96) and tend to be both structurally and functionally vulnerable in normal aging and Alzheimer's disease, which was suggested to be due to a high degree of life-long plasticity (32). The R2*- Aβ association points to an important relationship between brain microstructural properties reflected in tissue specific R2* measurements and the relationships between default activity, amyloid, and memory previously reported by Buckner et al (123). It is also in agreement with our previous consideration (12) that the cortical areas with lower R2t* (e.g., prefrontal cortex) may have more complex dendritic and synaptic structure, which may also be related to the neuroplasticity and AD vulnerability. From this perspective, the parahippocampal and entorhinal cortices, which are primary memory-related areas and are vulnerable to early Alzheimer, are also characterized by a lower baseline R2*. However, PiB retention and Aβ accumulation in these areas are not prominent. Nevertheless, the correlation between GEPCI R2* metrics and PiB retention in these areas is exceptionally strong, especially in the parahippocampal gyrus.

4.3.2 R2* Differentiates Normal and Preclinical AD Participants

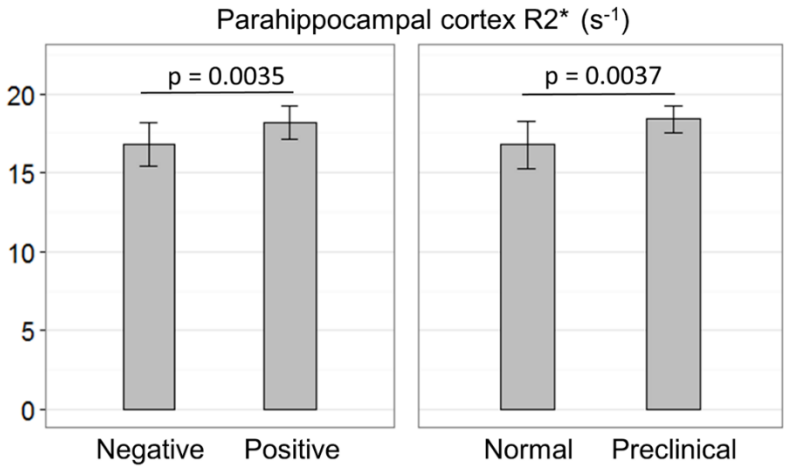

Figure 4.3 Group comparison based on R2* in the parahippocampal cortex. The bar graph on the left shows significant differences between participants with the negative (n = 15, R2* = 16.79 ± 1.40 s^{-1}) and the positive (n = 19, R2* = 18.20 ± 1.08 s^{-1}) Aβ status. The bar graph on the right shows significant differences between the normal group (CDR = 0, Aβ negative, n=13, R2* = 16.77 ± 1.51 s^{-1}) and the preclinical group (CDR = 0, Aβ positive, n = 10, R2* = 18.41 ± 0.84 s^{-1}).

Based on the strong correlation between Aβ SUVR and R2* in the parahippocampal cortex, R2* can potentially be used to distinguish the healthy stage from the preclinical AD as early AD is associated with Aβ accumulation (36, 39, 41, 42). Indeed, the bar graph on the left in Figure 4.3 shows a significant difference in the parahippocampal R2* between all participants with negative (n = 15) and positive (n = 19) Aβ status (independent of CDR, see definition in Methods). The bar graph on the right shows significant differences between normal group (CDR = 0, amyloid negative, n=13) and preclinical group (CDR = 0, Aβ positive, n = 10).

4.3.3 Correlation between R2t* and Cognitive Performance Tests

In Chapter 3, we compared GEPCI-derived tissue specific structural and functional metrics with existing literature and hypothesized that the parameter R2t* is related to the tissue neuronal density (12). As presented in the scatter plots in Figure 4.4, R2t* in the hippocampus was

associated with the free recall condition of the Free and Cued Selective Reminding Test (Srtfree; r = 0.53, p = 0.002), with the total correct score from the Animal Naming test (ANIMALS; r = 0.50, p = 0.0025), and with the Trailmaking Test Part A completion time (Tma; r = -0.47, p > 0.017). The decrease of R2t* is related to the neuronal damage in the hippocampus and so corresponds to a bad cognitive performance. But R2t* in the cortex doesn't significantly correlate with these three cognitive tests. This may be because the participants were characterized either as cognitively normal or having mild cognitive impairment (MCI), the neuronal damage (decreased R2t*) occurs first in the hippocampal area but may not spread to the cortical areas yet.

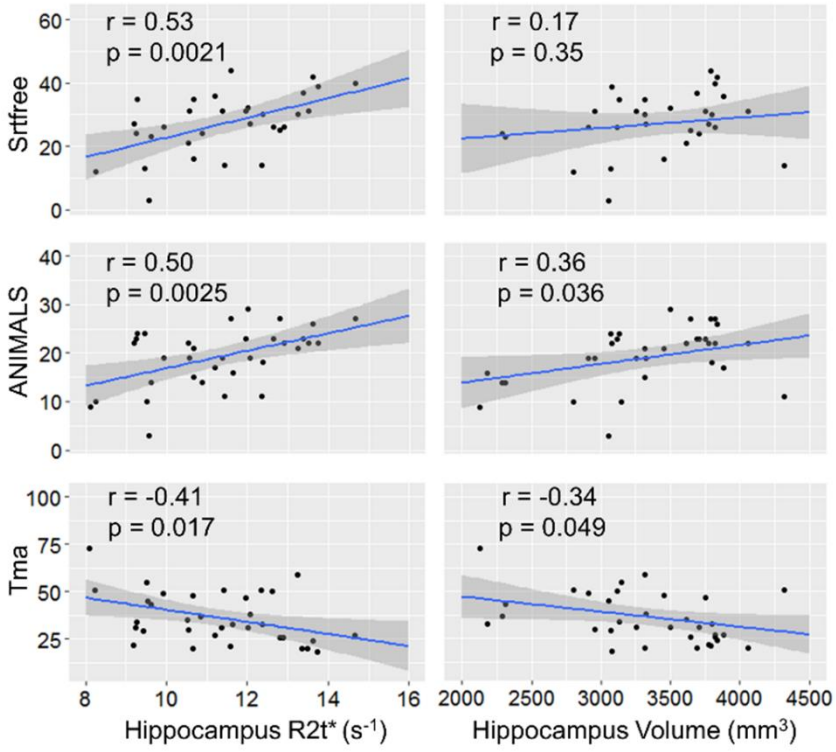

Figure 4.4 Correlation between cognitive tests performance and hippocampal R2t*. Cognitive measures included Free and Cued Selective Reminding Test (Srtfree), Animal Naming (ANIMALS), and Trail making Test Part A completion time (Tma). Note that higher scores on Tma indicate worse performance. Correlations with hippocampal volume are also presented for comparison. Each point represents a single participant (n = 34). Shaded areas represent 95%

confidence intervals of linear fits (solid lines). Pearson correlation coefficients (r) and p values are shown in the left upper corners.

Note that considerably weaker correlations were found between hippocampal volume and cognitive performance (Figure 4.4, second column), suggesting that the integrity of the remaining hippocampal tissue (characterized by R2t*) is a more important parameter of hippocampal pathology than hippocampal volume.

No significant correlation was found between cognitive performance and R2* or CSF $A\beta_{42}$. This result is in agreement with the dissociation between PiB defined Aβ plaques and cognitive performance (124-128). At least 30% of people with significant Aβ burden are cognitively normal (124).

4.3.4 R2t* Distinguishes Cognitively Normal Group from Mild AD Group

Figure 4.5 shows examples of three participants' GEPCI images from healthy control, preclinical and mild AD groups. Thin contours outline the hippocampus determined by FreeSurfer. In all cases, MPRAGE and GEPCI T1w images show small atrophy progressing from healthy to AD group. Gradually decreased R2t* suggest altered tissue integrity even in the preserved hippocampal area. One should keep in mind that GEPCI metrics (R2* and R2t*) are quantitative and provide information on tissue integrity based on comparison with healthy control measurements, thus uncovering tissue damage that might not be simply visible on images. Though tissue damage in the hippocampus can be clearly seen as hypointense signal on R2t* maps.

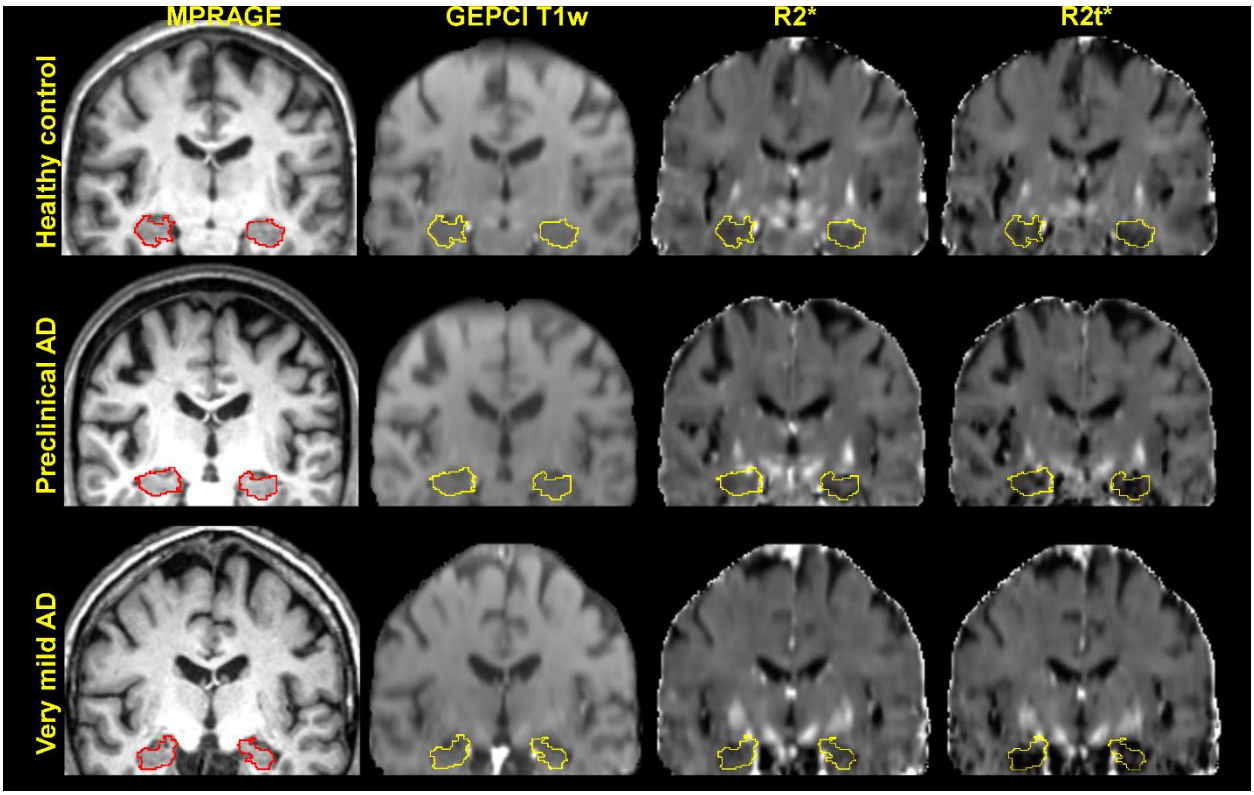

Figure 4.5 Examples of three participants' images – 69 year old female from the control group (upper row), 72 year old male from the preclinical AD group (second row) and 69 year old male from the mild AD (CDR = 0.5) group. Thin contours outline the hippocampus determined by FreeSurfer. In all cases, MPRAGE and GEPCI T1w images show small atrophy progressing from healthy to AD group. Gradually decreased GEPCI R2t* suggest altered tissue integrity even in the preserved hippocampal area.

The bar graphs in Figure 4.6 show group comparisons based on R2t* in the hippocampus. Three groups are shown - normal participants (CDR = 0, Aβ negative), preclinical group (CDR = 0, Aβ positive) and mild AD (CDR = 0.5 or 1). The first box shows results for tissue R2t* and the second block shows results for hippocampal volume. The significantly decreased hippocampal volume in mild AD group is in agreement with known brain atrophy characteristic for AD (109).

While changes in R2t* likely reflect changes in the neuronal and synaptic density, it may also reflect changes in other tissue components. Hypothetically, the slight but not significant increase in tissue R2t* seen in preclinical group as compared to normal participants in Figure 4.6 and

Table 4.3 may be attributed to accumulation of tau protein as in early Braak stages (105) of AD. Interestingly, Figure 4.6 and Table 4.3 also show that the hippocampal volume in the preclinical group was also slightly but not significantly higher than that in the normal group.

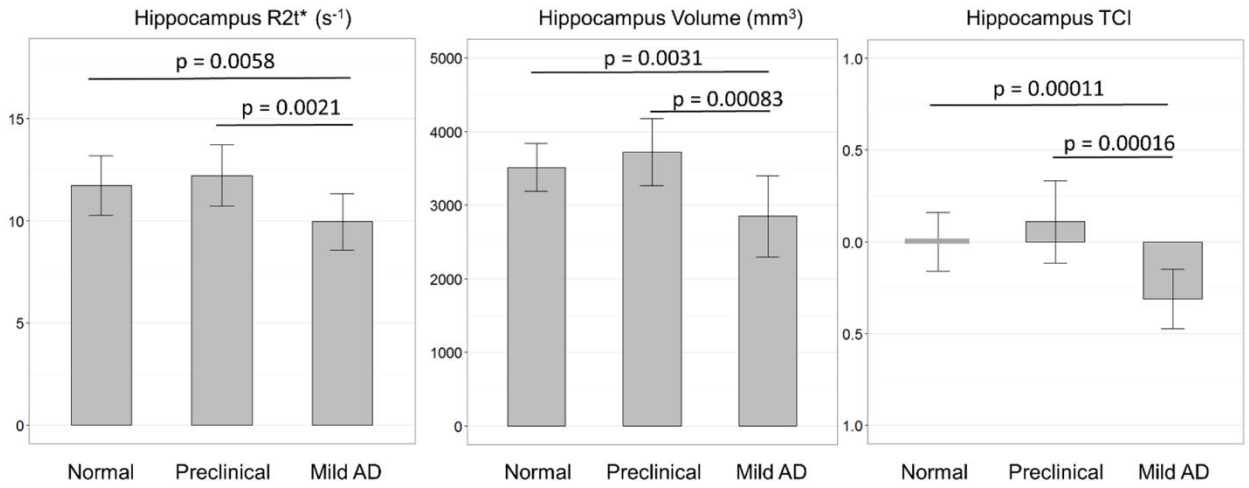

Figure 4.6 Bar graphs show the data obtained in the hippocampus of 34 participants. Bars represent mean values and error bars are standard deviations. Data are separated into three groups: Normal, preclinical AD, and mild AD (CDR 0.5 or 1). GEPCI R2t*, and volumes are shown. Also shown is the parameter TCI (tissue content index, Equation (4.3)). While R2t* can serve as a surrogate marker of neuronal density/integrity, the TCI can serve as a surrogate marker characterizing a change in the total neuronal content. The results are summarized in Table 4.3.

Table 4.3			
	R2t*(s^{-1})	Volume(mm^3)	TCI
Normal	11.71 ± 1.45	3512 ± 327	0.00 ± 0.16
Preclinical	12.20 ± 1.50	3720 ± 452	0.11 ± 0.22
Mild AD	9.94 ± 1.38	2849 ± 552	-0.31 ± 0.16

Table 4.3. The mean and standard deviations of R2t*, volume and TCI in hippocampus over three groups presented in Figure 4.6.

If R2t* is related to neuronal density/integrity, the product of R2t* and the hippocampal volume (*V*) could characterize the total neuronal content in the hippocampus. Hence, to characterize the global tissue change in the hippocampus, it is convenient to introduce the Tissue Content Index (TCI):

$$TCI = \frac{(V \cdot R2t^*) - (V \cdot R2t^*)_{control}}{(V \cdot R2t^*)_{control}} \qquad (4.3)$$

where $(V \cdot R2t^*)_{control}$ = 41201 $mm^3 \cdot sec^{-1}$ is a mean value of tissue content in the group of normal participants. The changes in the TCI between Normal, Preclinical and AD groups are shown in the third box of Figure 4.6.

The results in Figure 4.6 show that not only does the hippocampal tissue volume reduce in mild AD participants, but R2t* also reduces. As a result, the TCI reduce even more significantly. These results are in a full agreement with the histopathological studies of Price, Morris and co-workers (59) who found that 46% of neurons were lost in the hippocampus of people with CDR = 0.5 as compared to cognitively normal participants, while the hippocampal volume loss was only 29%. Comparison of our findings with direct neuronal measurements in (59) further confirms our hypothesized relationship between R2t* and neuronal density. The decreased R2t* and TCI is consistent with decreased tissue neuronal density and the tissue neuronal content in the hippocampus. Furthermore, no significant differences in hippocampal R2t*, volume and TCI between the normal and preclinical AD groups, is also consistent with Price, Morris and co-workers' finding of no significant difference in hippocampal neuron number and volume between the normal and preclinical AD groups (59).

4.4 Summary

In this study, we have demonstrated that the GEPCI technique provides a new approach to the *in vivo* evaluation of pathology in the preclinical and early symptomatic stages of AD. It is based on a multi-gradient-echo MRI sequence that is available from most MRI manufacturers. GEPCI data are quantitative, reproducible and MRI scanner independent, thus allowing multi-center applications. The results show that GEPCI metrics are good correlates of Aβ accumulation and neurodegeneration. They are sensitive enough to distinguish between normal individuals and those with preclinical (asymptomatic) and early symptomatic AD.

One of the significant conclusions of this study is that the tissue cellular integrity of the preserved part of the hippocampus is a more important parameter affecting cognitive performance than the hippocampal atrophy. This points out to the presence of significant cognitive reserve in the hippocampal structure. Another important finding is that the AD symptoms do not start until there has been significant cellular loss in the hippocampus identified by GEPCI metrics, consistent with Price, Morris and colleagues (59).

Since MRI is a much more available modality than PET (current imaging "gold standard" for *in vivo* quantifying AD (Aβ) brain pathology), and poses fewer risks, GEPCI metrics (R2* and R2t*) have a potential for improving the quality of AD diagnostic measures, and the evaluation of new disease-modifying therapies.

The results of this study are based on data obtained from 34 participants. Larger and independent samples certainly should be used to further validate our findings.

Chapter 5: Future Plan

Last but not least, the GEPCI approach has been used to study many cognitive disease. For example, GEPCI has been used to identify brain tissue damage in multiple sclerosis (2, 4, 69-72) and psychiatric diseases (73). R2* has been found to be significantly lower in patients with multiple sclerosis (MS) than in healthy participants (2, 4, 69-72). Significant correlations between age-adjusted R2* and clinical scores of MS have been reported for cortical regions (71). Significant group effects based on GEPCI metrics have been observed in the superior temporal cortex and in the thalamus of the participants with schizophrenia and bipolar disorder (73). In this dissertation, the GEPCI approach has been applied to normal aging and Alzheimer's disease. Thus, there is a potential for the GEPCI approach to provide insightful information about cognitive disease. Certainly, more experimental data should be investigated to validate this approach. The following ideas may be considered as future directions:

1. More participants with various amounts of amyloid deposition should be recruited to further validate the correlation between the PET biomarker retention of amyloid deposition and GEPCI R2*.
2. More participants with CDR = 0, 0.5, and 1 should be recruited to further validate the correlation between the cognitive performance tests and the GEPCI hippocampal R2t*, and to further validate the ability of R2t* to distinguish cognitively normal and mild AD groups.
3. A recent study reports the detection of tau deposition *in vivo* using PET imaging (54). Similar correlations between PET biomarker retentions of tau and GEPCI metrics (e.g., R2* and R2t*) should be investigated.

4. Examine the autopsy of participants who underwent GEPCI MRI prior to expiration. Also investigate the histological results and GEPCI results. For example, investigate the relationship between neuronal density and GEPCI R2t*.
5. Interestingly, supervised machine-learning classification and cross-validation algorithms may be applied to quantitative GEPCI measurements to classify volunteers' condition with respect to Alzheimer's disease if a large dataset is available. Because deep learning has been widely used in image processing, it is interesting to apply deep-learning algorithms directly to MRI images for classification.

References

1. Yablonskiy DA (2000) Quntitative T2 contrast with Gradient Echoes. in *8th Annual Meeting of the International Society for Magnetic Resonance in Medicine* (Denver, Colorado).
2. Luo J, Jagadeesan BD, Cross AH, & Yablonskiy DA (2012) Gradient Echo Plural Contrast Imaging - Signal model and derived contrasts: T2*, T1, Phase, SWI, T1f, FST2*and T2*-SWI. *NeuroImage* 60(2):1073-1082.
3. Yablonskiy DA, Sukstanskii AL, Luo J, & Wang X (2013) Voxel spread function method for correction of magnetic field inhomogeneity effects in quantitative gradient-echo-based MRI. *Magnetic resonance in medicine : official journal of the Society of Magnetic Resonance in Medicine / Society of Magnetic Resonance in Medicine* 70(5):1283-1292.
4. Wen J, Cross AH, & Yablonskiy DA (2014) On the role of physiological fluctuations in quantitative gradient echo MRI: implications for GEPCI, QSM, and SWI. *Magnetic resonance in medicine : official journal of the Society of Magnetic Resonance in Medicine / Society of Magnetic Resonance in Medicine*.
5. Ulrich X & Yablonskiy DA (2015) Separation of cellular and BOLD contributions to T2* signal relaxation. *Magnetic resonance in medicine : official journal of the Society of Magnetic Resonance in Medicine / Society of Magnetic Resonance in Medicine*.
6. Luo J, Jagadeesan BD, Cross AH, & Yablonskiy DA (2012) Gradient echo plural contrast imaging--signal model and derived contrasts: T2*, T1, phase, SWI, T1f, FST2*and T2*-SWI. *NeuroImage* 60(2):1073-1082.
7. Quirk JD, Sukstanskii AL, Bretthorst GL, & Yablonskiy DA (2009) Optimal decay rate constant estimates from phased array data utilizing joint Bayesian analysis. *J Magn Reson* 198(1):49-56.
8. Yablonskiy DA (1998) Quantitation of intrinsic magnetic susceptibility-related effects in a tissue matrix. Phantom study. *Magnetic Resonance in Medicine* 39(3):417-428.
9. Ogawa S, Lee TM, Kay AR, & Tank DW (1990) Brain magnetic resonance imaging with contrast dependent on blood oxygenation. *Proceedings of the National Academy of Sciences of the United States of America* 87(24):9868-9872.
10. Mintun MA, Raichle ME, Martin WR, & Herscovitch P (1984) Brain oxygen utilization measured with O-15 radiotracers and positron emission tomography. *Journal of nuclear medicine : official publication, Society of Nuclear Medicine* 25(2):177-187.
11. Yablonskiy DA & Haacke EM (1994) Theory of NMR signal behavior in magnetically inhomogeneous tissues: the static dephasing regime. *Magnetic resonance in medicine : official journal of the Society of Magnetic Resonance in Medicine / Society of Magnetic Resonance in Medicine* 32(6):749-763.
12. Zhao Y, Wen J, Cross AH, & Yablonskiy DA (2016) On the relationship between cellular and hemodynamic properties of the human brain cortex throughout adult lifespan. *NeuroImage* 133:417-429.
13. Spees WM, Yablonskiy DA, Oswood MC, & Ackerman JJ (2001) Water proton MR properties of human blood at 1.5 Tesla: magnetic susceptibility, T(1), T(2), T*(2), and non-Lorentzian signal behavior. *Magnetic resonance in medicine : official journal of the*

Society of Magnetic Resonance in Medicine / Society of Magnetic Resonance in Medicine 45(4):533-542.
14. He X, Zhu M, & Yablonskiy DA (2008) Validation of oxygen extraction fraction measurement by qBOLD technique. *Magnetic resonance in medicine : official journal of the Society of Magnetic Resonance in Medicine / Society of Magnetic Resonance in Medicine* 60(4):882-888.
15. Dickson JD, *et al.* (2011) Quantitative phenomenological model of the BOLD contrast mechanism. *J Magn Reson* 212(1):17-25.
16. Wang X, Sukstanskii AL, & Yablonskiy DA (2013) Optimization strategies for evaluation of brain hemodynamic parameters with qBOLD technique. *Magnetic resonance in medicine : official journal of the Society of Magnetic Resonance in Medicine / Society of Magnetic Resonance in Medicine* 69(4):1034-1043.
17. Yablonskiy DA, Sukstanskii AL, & He X (2013) Blood oxygenation level-dependent (BOLD)-based techniques for the quantification of brain hemodynamic and metabolic properties - theoretical models and experimental approaches. *NMR Biomed* 26(8):963-986.
18. He X & Yablonskiy DA (2007) Quantitative BOLD: mapping of human cerebral deoxygenated blood volume and oxygen extraction fraction: default state. *Magnetic resonance in medicine : official journal of the Society of Magnetic Resonance in Medicine / Society of Magnetic Resonance in Medicine* 57(1):115-126.
19. Morrison JH & Hof PR (1997) Life and death of neurons in the aging brain. *Science* 278(5337):412-419.
20. Brody H (1955) Organization of the cerebral cortex. III. A study of aging in the human cerebral cortex. *The Journal of comparative neurology* 102(2):511-516.
21. Coleman PD & Flood DG (1987) Neuron numbers and dendritic extent in normal aging and Alzheimer's disease. *Neurobiology of aging* 8(6):521-545.
22. Terry RD, DeTeresa R, & Hansen LA (1987) Neocortical cell counts in normal human adult aging. *Annals of neurology* 21(6):530-539.
23. Haug H & Eggers R (1991) Morphometry of the human cortex cerebri and corpus striatum during aging. *Neurobiology of aging* 12(4):336-338; discussion 352-335.
24. Pakkenberg B & Gundersen HJ (1997) Neocortical neuron number in humans: effect of sex and age. *The Journal of comparative neurology* 384(2):312-320.
25. Pakkenberg B, *et al.* (2003) Aging and the human neocortex. *Experimental gerontology* 38(1-2):95-99.
26. Freeman SH, *et al.* (2008) Preservation of neuronal number despite age-related cortical brain atrophy in elderly subjects without Alzheimer disease. *Journal of neuropathology and experimental neurology* 67(12):1205-1212.
27. Pelvig DP, Pakkenberg H, Stark AK, & Pakkenberg B (2008) Neocortical glial cell numbers in human brains. *Neurobiology of aging* 29(11):1754-1762.
28. Scahill RI, *et al.* (2003) A longitudinal study of brain volume changes in normal aging using serial registered magnetic resonance imaging. *Archives of neurology* 60(7):989-994.
29. Fotenos AF, Snyder AZ, Girton LE, Morris JC, & Buckner RL (2005) Normative estimates of cross-sectional and longitudinal brain volume decline in aging and AD. *Neurology* 64(6):1032-1039.

30. Salat DH, *et al.* (2004) Thinning of the cerebral cortex in aging. *Cereb Cortex* 14(7):721-730.
31. Haug H (1985) Are Neurons of the Human Cerebral-Cortex Lost during Aging. *Nervenheilkunde* 4(2):103-109.
32. Fjell AM, McEvoy L, Holland D, Dale AM, & Walhovd KB (2014) What is normal in normal aging? Effects of aging, amyloid and Alzheimer's disease on the cerebral cortex and the hippocampus. *Progress in neurobiology* 117:20-40.
33. Dickstein DL, Weaver CM, Luebke JI, & Hof PR (2013) Dendritic spine changes associated with normal aging. *Neuroscience* 251:21-32.
34. Hof PR & Morrison JH (2004) The aging brain: morphomolecular senescence of cortical circuits. *Trends in neurosciences* 27(10):607-613.
35. Morrison JH & Baxter MG (2012) The ageing cortical synapse: hallmarks and implications for cognitive decline. *Nature reviews. Neuroscience* 13(4):240-250.
36. Jack CR, Jr., *et al.* (2010) Hypothetical model of dynamic biomarkers of the Alzheimer's pathological cascade. *Lancet neurology* 9(1):119-128.
37. Albert MS, *et al.* (2011) The diagnosis of mild cognitive impairment due to Alzheimer's disease: Recommendations from the National Institute on Aging-Alzheimer's Association workgroups on diagnostic guidelines for Alzheimer's disease. *Alzheimer's & Dementia* 7(3):270-279.
38. McKhann GM, *et al.* (2011) The diagnosis of dementia due to Alzheimer's disease: Recommendations from the National Institute on Aging-Alzheimer's Association workgroups on diagnostic guidelines for Alzheimer's disease. *Alzheimer's & Dementia* 7(3):263-269.
39. Selkoe DJ (1991) Alzheimer's disease. In the beginning. *Nature* 354(6353):432-433.
40. Hardy J & Allsop D (1991) Amyloid deposition as the central event in the aetiology of Alzheimer's disease. *Trends Pharmacol Sci* 12(10):383-388.
41. Hardy JA & Higgins GA (1992) Alzheimer's disease: the amyloid cascade hypothesis. *Science* 256(5054):184-185.
42. Hardy J & Selkoe DJ (2002) The amyloid hypothesis of Alzheimer's disease: progress and problems on the road to therapeutics. *Science* 297(5580):353-356.
43. Bateman RJ, *et al.* (2012) Clinical and biomarker changes in dominantly inherited Alzheimer's disease. *The New England journal of medicine* 367(9):795-804.
44. Benzinger TL, *et al.* (2013) Regional variability of imaging biomarkers in autosomal dominant Alzheimer's disease. *Proceedings of the National Academy of Sciences of the United States of America* 110(47):E4502-4509.
45. Sperling RA, *et al.* (2011) Toward defining the preclinical stages of Alzheimer's disease: recommendations from the National Institute on Aging-Alzheimer's Association workgroups on diagnostic guidelines for Alzheimer's disease. *Alzheimer's & dementia : the journal of the Alzheimer's Association* 7(3):280-292.
46. Kang J, *et al.* (1987) The precursor of Alzheimer's disease amyloid A4 protein resembles a cell-surface receptor. *Nature* 325(6106):733-736.
47. Klunk WE, *et al.* (2004) Imaging brain amyloid in Alzheimer's disease with Pittsburgh Compound-B. *Annals of neurology* 55(3):306-319.
48. Price JC, *et al.* (2005) Kinetic modeling of amyloid binding in humans using PET imaging and Pittsburgh Compound-B. *Journal of cerebral blood flow and metabolism :*

official journal of the International Society of Cerebral Blood Flow and Metabolism 25(11):1528-1547.
49. Ikonomovic MD, *et al.* (2008) Post-mortem correlates of in vivo PiB-PET amyloid imaging in a typical case of Alzheimer's disease. *Brain : a journal of neurology* 131(Pt 6):1630-1645.
50. Fagan AM, *et al.* (2006) Inverse relation between in vivo amyloid imaging load and cerebrospinal fluid Abeta42 in humans. *Annals of neurology* 59(3):512-519.
51. Villain N, *et al.* (2012) Regional dynamics of amyloid-beta deposition in healthy elderly, mild cognitive impairment and Alzheimer's disease: a voxelwise PiB-PET longitudinal study. *Brain : a journal of neurology* 135(Pt 7):2126-2139.
52. Bennett DA, Schneider JA, Wilson RS, Bienias JL, & Arnold SE (2004) Neurofibrillary tangles mediate the association of amyloid load with clinical Alzheimer disease and level of cognitive function. *Archives of neurology* 61(3):378-384.
53. Giannakopoulos P, *et al.* (2003) Tangle and neuron numbers, but not amyloid load, predict cognitive status in Alzheimer's disease. *Neurology* 60(9):1495-1500.
54. Brier MR, *et al.* (2016) Tau and Abeta imaging, CSF measures, and cognition in Alzheimer's disease. *Science translational medicine* 8(338):338ra366.
55. Savva GM, *et al.* (2009) Age, neuropathology, and dementia. *The New England journal of medicine* 360(22):2302-2309.
56. Whitwell JL, *et al.* (2008) MRI correlates of neurofibrillary tangle pathology at autopsy: a voxel-based morphometry study. *Neurology* 71(10):743-749.
57. Schuff N, *et al.* (2009) MRI of hippocampal volume loss in early Alzheimer's disease in relation to ApoE genotype and biomarkers. *Brain : a journal of neurology* 132(Pt 4):1067-1077.
58. Jack CR, Jr., *et al.* (2000) Rates of hippocampal atrophy correlate with change in clinical status in aging and AD. *Neurology* 55(4):484-489.
59. Price JL, *et al.* (2001) Neuron number in the entorhinal cortex and CA1 in preclinical Alzheimer disease. *Archives of neurology* 58(9):1395-1402.
60. Gomez-Isla T, *et al.* (1996) Profound loss of layer II entorhinal cortex neurons occurs in very mild Alzheimer's disease. *The Journal of neuroscience : the official journal of the Society for Neuroscience* 16(14):4491-4500.
61. Juottonen K, Lehtovirta M, Helisalmi S, Riekkinen PJ, Sr., & Soininen H (1998) Major decrease in the volume of the entorhinal cortex in patients with Alzheimer's disease carrying the apolipoprotein E epsilon4 allele. *Journal of neurology, neurosurgery, and psychiatry* 65(3):322-327.
62. West MJ, Kawas CH, Stewart WF, Rudow GL, & Troncoso JC (2004) Hippocampal neurons in pre-clinical Alzheimer's disease. *Neurobiology of aging* 25(9):1205-1212.
63. Burgmans S, *et al.* (2011) The posterior parahippocampal gyrus is preferentially affected in age-related memory decline. *Neurobiology of aging* 32(9):1572-1578.
64. Echavarri C, *et al.* (2011) Atrophy in the parahippocampal gyrus as an early biomarker of Alzheimer's disease. *Brain structure & function* 215(3-4):265-271.
65. Thangavel R, Van Hoesen GW, & Zaheer A (2008) Posterior parahippocampal gyrus pathology in Alzheimer's disease. *Neuroscience* 154(2):667-676.
66. Arnold SE, Hyman BT, Flory J, Damasio AR, & Van Hoesen GW (1991) The topographical and neuroanatomical distribution of neurofibrillary tangles and neuritic

plaques in the cerebral cortex of patients with Alzheimer's disease. *Cereb Cortex* 1(1):103-116.
67. Morris JC (1993) The Clinical Dementia Rating (CDR): current version and scoring rules. *Neurology* 43(11):2412-2414.
68. Bobinski M, *et al.* (2000) The histological validation of post mortem magnetic resonance imaging-determined hippocampal volume in Alzheimer's disease. *Neuroscience* 95(3):721-725.
69. Sati P, Cross AH, Luo J, Hildebolt CF, & Yablonskiy DA (2010) In vivo quantitative evaluation of brain tissue damage in multiple sclerosis using gradient echo plural contrast imaging technique. *NeuroImage* 51(3):1089-1097.
70. Luo J, Yablonskiy DA, Hildebolt CF, Lancia S, & Cross AH (2014) Gradient echo magnetic resonance imaging correlates with clinical measures and allows visualization of veins within multiple sclerosis lesions. *Mult Scler* 20(3):349-355.
71. Wen J, *et al.* (2015) Detection and quantification of regional cortical gray matter damage in multiple sclerosis utilizing gradient echo MRI. *NeuroImage: Clinical* 9:164-175.
72. Patel KR, *et al.* (2015) Detection of cortical lesions in multiple sclerosis: A new imaging approach. *Multiple Sclerosis Journal – Experimental, Translational and Clinical* 1.
73. Mamah D, *et al.* (2015) Subcomponents of brain T2* relaxation in schizophrenia, bipolar disorder and siblings: A Gradient Echo Plural Contrast Imaging (GEPCI) study. *Schizophr Res*.
74. Zhao Y, *et al.* (2016) In vivo detection of microstructural correlates of brain pathology in preclinical and early Alzheimer Disease with magnetic resonance imaging. *NeuroImage* 148:296-304.
75. Mugler JP & Brookeman JR (1990) Three-dimensional magnetization-prepared rapid gradient-echo imaging (3D MP RAGE). *Magn.Reson.Med.* 15(1):152-157.
76. Reuter M, Schmansky NJ, Rosas HD, & Fischl B (2012) Within-subject template estimation for unbiased longitudinal image analysis. *NeuroImage* 61(4):1402-1418.
77. Jenkinson M, Beckmann CF, Behrens TEJ, Woolrich MW, & Smith SM (2012) FSL. *NeuroImage* 62(2):782-790.
78. Jenkinson M, Bannister P, Brady M, & Smith S (2002) Improved Optimization for the Robust and Accurate Linear Registration and Motion Correction of Brain Images. *NeuroImage* 17(2):825-841.
79. Cohen-Adad J (2014) What can we learn from T2* maps of the cortex? *NeuroImage* 93 Pt 2:189-200.
80. Stuber C, *et al.* (2014) Myelin and iron concentration in the human brain: A quantitative study of MRI contrast. *NeuroImage* 93P1:95-106.
81. Fukunaga M, *et al.* (2010) Layer-specific variation of iron content in cerebral cortex as a source of MRI contrast. *Proceedings of the National Academy of Sciences of the United States of America* 107(8):3834-3839.
82. Haacke EM, *et al.* (2005) Imaging iron stores in the brain using magnetic resonance imaging. *Magnetic resonance imaging* 23(1):1-25.
83. Peran P, *et al.* (2009) Volume and iron content in basal ganglia and thalamus. *Human brain mapping* 30(8):2667-2675.
84. Sedlacik J, *et al.* (2014) Reversible, irreversible and effective transverse relaxation rates in normal aging brain at 3T. *NeuroImage* 84:1032-1041.

85. Gelman N, *et al.* (1999) MR imaging of human brain at 3.0 T: preliminary report on transverse relaxation rates and relation to estimated iron content. *Radiology* 210(3):759-767.
86. Yao B, *et al.* (2009) Susceptibility contrast in high field MRI of human brain as a function of tissue iron content. *NeuroImage* 44(4):1259-1266.
87. Langkammer C, *et al.* (2010) Quantitative MR imaging of brain iron: a postmortem validation study. *Radiology* 257(2):455-462.
88. Hallgren B & Sourander P (1958) The effect of age on the non-haemin iron in the human brain. *Journal of neurochemistry* 3(1):41-51.
89. Rudko DA, *et al.* (2014) Origins of R2* orientation dependence in gray and white matter. *Proceedings of the National Academy of Sciences of the United States of America* 111(1):E159-167.
90. Seewann A, *et al.* (2009) Diffusely abnormal white matter in chronic multiple sclerosis: imaging and histopathologic analysis. *Archives of neurology* 66(5):601-609.
91. He X & Yablonskiy DA (2009) Biophysical mechanisms of phase contrast in gradient echo MRI. *Proceedings of the National Academy of Sciences of the United States of America* 106(32):13558-13563.
92. Hedden T & Gabrieli JD (2004) Insights into the ageing mind: a view from cognitive neuroscience. *Nature reviews. Neuroscience* 5(2):87-96.
93. Collins CE, Airey DC, Young NA, Leitch DB, & Kaas JH (2010) Neuron densities vary across and within cortical areas in primates. *Proceedings of the National Academy of Sciences of the United States of America* 107(36):15927-15932.
94. Elston GN, Benavides-Piccione R, & DeFelipe J (2001) The pyramidal cell in cognition: a comparative study in human and monkey. *The Journal of neuroscience : the official journal of the Society for Neuroscience* 21(17):RC163.
95. Glasser MF & Van Essen DC (2011) Mapping human cortical areas in vivo based on myelin content as revealed by T1- and T2-weighted MRI. *The Journal of neuroscience : the official journal of the Society for Neuroscience* 31(32):11597-11616.
96. Raichle ME, *et al.* (2001) A default mode of brain function. *Proceedings of the National Academy of Sciences of the United States of America* 98(2):676-682.
97. Leenders KL, *et al.* (1990) Cerebral blood flow, blood volume and oxygen utilization. Normal values and effect of age. *Brain : a journal of neurology* 113 (Pt 1):27-47.
98. Pantano P, *et al.* (1984) Regional cerebral blood flow and oxygen consumption in human aging. *Stroke; a journal of cerebral circulation* 15(4):635-641.
99. Yamaguchi T, *et al.* (1986) Reduction in regional cerebral metabolic rate of oxygen during human aging. *Stroke; a journal of cerebral circulation* 17(6):1220-1228.
100. Vlassenko AG, *et al.* (2010) Spatial correlation between brain aerobic glycolysis and amyloid-beta (Abeta) deposition. *Proceedings of the National Academy of Sciences of the United States of America* 107(41):17763-17767.
101. Vaishnavi SN, *et al.* (2010) Regional aerobic glycolysis in the human brain. *Proceedings of the National Academy of Sciences of the United States of America* 107(41):17757-17762.
102. Morris JC, *et al.* (2012) Developing an international network for Alzheimer research: The Dominantly Inherited Alzheimer Network. *Clinical investigation* 2(10):975-984.

103. Fagan AM, Csernansky CA, Morris JC, & Holtzman DM (2005) The search for antecedent biomarkers of Alzheimer's disease. *Journal of Alzheimer's disease : JAD* 8(4):347-358.
104. Reiman EM, *et al.* (2016) CAP--advancing the evaluation of preclinical Alzheimer disease treatments. *Nature reviews. Neurology* 12(1):56-61.
105. Braak H & Braak E (1991) Neuropathological stageing of Alzheimer-related changes. *Acta neuropathologica* 82(4):239-259.
106. Mitchell TW, *et al.* (2002) Parahippocampal tau pathology in healthy aging, mild cognitive impairment, and early Alzheimer's disease. *Annals of neurology* 51(2):182-189.
107. Hyman BT, Van Hoesen GW, Damasio AR, & Barnes CL (1984) Alzheimer's disease: cell-specific pathology isolates the hippocampal formation. *Science* 225(4667):1168-1170.
108. Price JL & Morris JC (1999) Tangles and plaques in nondemented aging and "preclinical" Alzheimer's disease. *Annals of neurology* 45(3):358-368.
109. Dickerson BC, *et al.* (2011) Alzheimer-signature MRI biomarker predicts AD dementia in cognitively normal adults. *Neurology* 76(16):1395-1402.
110. Benveniste H, Einstein G, Kim KR, Hulette C, & Johnson GA (1999) Detection of neuritic plaques in Alzheimer's disease by magnetic resonance microscopy. *Proceedings of the National Academy of Sciences* 96(24):14079-14084.
111. Meadowcroft MD, Connor JR, Smith MB, & Yang QX (2009) MRI and histological analysis of beta-amyloid plaques in both human Alzheimer's disease and APP/PS1 transgenic mice. *Journal of Magnetic Resonance Imaging* 29(5):997-1007.
112. Wengenack TM, *et al.* (2011) Regional differences in MRI detection of amyloid plaques in AD transgenic mouse brain. *NeuroImage* 54(1):113-122.
113. Chamberlain R, *et al.* (2009) Comparison of amyloid plaque contrast generated by T2-weighted, T 2*-weighted, and susceptibility-weighted imaging methods in transgenic mouse models of Alzheimer's disease. *Magnetic Resonance in Medicine* 61(5):1158-1164.
114. Lee S-P, Falangola MF, Nixon RA, Duff K, & Helpern JA (2004) Visualization of β-amyloid plaques in a transgenic mouse model of Alzheimer's disease using MR microscopy without contrast reagents. *Magnetic Resonance in Medicine* 52(3):538-544.
115. Maier FC, *et al.* (2015) Quantification of beta-Amyloidosis and rCBF with Dedicated PET, 7 T MR Imaging, and High-Resolution Microscopic MR Imaging at 16.4 T in APP23 Mice. *Journal of nuclear medicine : official publication, Society of Nuclear Medicine* 56(10):1593-1599.
116. Johnson DK, Storandt M, Morris JC, Langford ZD, & Galvin JE (2008) Cognitive profiles in dementia: Alzheimer disease vs healthy brain aging. *Neurology* 71(22):1783-1789.
117. Mintun MA, *et al.* (2006) [11C]PIB in a nondemented population: potential antecedent marker of Alzheimer disease. *Neurology* 67(3):446-452.
118. Benjamini Y & Hochberg Y (1995) Controlling the False Discovery Rate: A Practical and Powerful Approach to Multiple Testing. *Journal of the Royal Statistical Society. Series B (Methodological)* 57(1):289-300.
119. Hoesen GWV (2002) The human parahippocampal region in Alzheimer's disease, dementia, and ageing. *The parahippocampal region : organization and role in cognitive*

function, eds Witter MP & Wouterlood FG (Oxford University Press, Oxford; New York).
120. Scharfman HE, Witter MP, & Schwarcz R (2000) Preface. *Annals of the New York Academy of Sciences* 911(1):ix-xiii.
121. Duyn JH (2012) The future of ultra-high field MRI and fMRI for study of the human brain. *NeuroImage* 62(2):1241-1248.
122. Su Y, *et al.* (2013) Quantitative analysis of PiB-PET with FreeSurfer ROIs. *PloS one* 8(11):e73377.
123. Buckner RL, *et al.* (2005) Molecular, structural, and functional characterization of Alzheimer's disease: evidence for a relationship between default activity, amyloid, and memory. *The Journal of neuroscience : the official journal of the Society for Neuroscience* 25(34):7709-7717.
124. Morris JC, *et al.* (2009) Pittsburgh compound B imaging and prediction of progression from cognitive normality to symptomatic Alzheimer disease. *Archives of neurology* 66(12):1469-1475.
125. Price JL, *et al.* (2009) Neuropathology of nondemented aging: presumptive evidence for preclinical Alzheimer disease. *Neurobiology of aging* 30(7):1026-1036.
126. Elman JA, *et al.* (2014) Neural compensation in older people with brain amyloid-beta deposition. *Nature neuroscience* 17(10):1316-1318.
127. Rentz DM, *et al.* (2010) Cognition, reserve, and amyloid deposition in normal aging. *Annals of neurology* 67(3):353-364.
128. Wirth M, *et al.* (2013) Alzheimer's disease neurodegenerative biomarkers are associated with decreased cognitive function but not beta-amyloid in cognitively normal older individuals. *The Journal of neuroscience : the official journal of the Society for Neuroscience* 33(13):5553-5563.

Chapter 3 is reprinted from Neuroimage, Vol 133, Zhao Y, Wen J, Cross AH, & Yablonskiy DA, On the relationship between cellular and hemodynamic properties of the human brain cortex throughout adult lifespan, p. 417-29, 2016, with permission from Elsevier.

Chapter 4 is reprinted from NeuroImage, Vol 148, Zhao Y, *et al.* (2016) In vivo detection of microstructural correlates of brain pathology in preclinical and early Alzheimer Disease with magnetic resonance imaging. P. 296-304, 2016, with permissio from Elsevier.